

## Phase-transformation and precipitation kinetics in vanadium micro-alloyed steels by in-situ, simultaneous neutron diffraction and SANS

Ioannidou, Chrysoula; Navarro-López, Alfonso; Dalglish, Robert M.; Rijkenberg, Arjan; Geerlofs, Nico; Pappas, Catherine; Sietsma, Jilt; van Well, Ad A.; Offerman, S. Erik; More Authors

**DOI**

[10.1016/j.actamat.2021.117317](https://doi.org/10.1016/j.actamat.2021.117317)

**Publication date**

2021

**Document Version**

Final published version

**Published in**

Acta Materialia

**Citation (APA)**

Ioannidou, C., Navarro-López, A., Dalglish, R. M., Rijkenberg, A., Geerlofs, N., Pappas, C., Sietsma, J., van Well, A. A., Offerman, S. E., & More Authors (2021). Phase-transformation and precipitation kinetics in vanadium micro-alloyed steels by in-situ, simultaneous neutron diffraction and SANS. *Acta Materialia*, 220, Article 117317. <https://doi.org/10.1016/j.actamat.2021.117317>

**Important note**

To cite this publication, please use the final published version (if applicable). Please check the document version above.

**Copyright**

Other than for strictly personal use, it is not permitted to download, forward or distribute the text or part of it, without the consent of the author(s) and/or copyright holder(s), unless the work is under an open content license such as Creative Commons.

**Takedown policy**

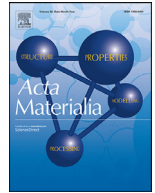
Please contact us and provide details if you believe this document breaches copyrights. We will remove access to the work immediately and investigate your claim.



ELSEVIER

Contents lists available at ScienceDirect

Acta Materialia

journal homepage: [www.elsevier.com/locate/actamat](http://www.elsevier.com/locate/actamat)

Full Length Article

# Phase-transformation and precipitation kinetics in vanadium micro-alloyed steels by *in-situ*, simultaneous neutron diffraction and SANS



Chrysoula Ioannidou<sup>a,1,\*</sup>, Alfonso Navarro-López<sup>a</sup>, Robert M. Dalglish<sup>b</sup>, Arjan Rijkenberg<sup>c</sup>, Xukai Zhang<sup>d,2</sup>, Bart Kooi<sup>d</sup>, Nico Geerlofs<sup>a</sup>, Catherine Pappas<sup>e</sup>, Jilt Sietsma<sup>a</sup>, Ad A. van Well<sup>e</sup>, S. Erik Offerman<sup>a,\*</sup>

<sup>a</sup> Department of Materials Science and Engineering, Delft University of Technology, Mekelweg 2, Delft 2628 CD, the Netherlands

<sup>b</sup> STFC, ISIS, Rutherford Appleton Laboratory, Chilton, Oxfordshire OX11 0QX, United Kingdom

<sup>c</sup> Tata Steel, 1970 CA, IJmuiden, the Netherlands

<sup>d</sup> Zernike Institute for Advanced Materials, University of Groningen, Nijenborgh 4, Groningen 9747 AG, the Netherlands

<sup>e</sup> Department of Radiation Science and Technology, Faculty of Applied Sciences, Delft University of Technology, Mekelweg 15, Delft 2629 JB, the Netherlands

## ARTICLE INFO

### Article history:

Received 11 July 2021

Revised 10 September 2021

Accepted 13 September 2021

Available online 17 September 2021

Edited by Dr T Furuwara

### Keywords:

In-situ measurements

Small-Angle Neutron Scattering

Neutron Diffraction

Vanadium micro-alloyed steels

Phase-transformation and precipitation

kinetics

## ABSTRACT

*In-situ* Neutron Diffraction and Small-Angle Neutron Scattering (SANS) are employed for the first time simultaneously in order to reveal the interaction between the austenite to ferrite phase transformation and the precipitation kinetics during isothermal annealing at 650 and at 700 °C in three steels with different vanadium (V) and carbon (C) concentrations. Austenite-to-ferrite phase transformation is observed in all three steels at both temperatures. The phase transformation is completed during a 10 h annealing treatment in all cases. The phase transformation is faster at 650 than at 700 °C for all alloys. Additions of vanadium and carbon to the steel composition cause a retardation of the phase transformation. The effect of each element is explained through its contribution to the Gibbs free energy dissipation. The austenite-to-ferrite phase transformation is found to initiate the vanadium carbide precipitation. Larger and fewer precipitates are detected at 700 than at 650 °C in all three steels, and a larger number density of precipitates is detected in the steel with higher concentrations of vanadium and carbon. After 10 h of annealing, the precipitated phase does not reach the equilibrium fraction as calculated by ThermoCalc. The external magnetic field applied during the experiments, necessary for the SANS measurements, causes a delay in the onset and time evolution of the austenite-to-ferrite phase transformation and consequently on the precipitation kinetics.

© 2021 The Author(s). Published by Elsevier Ltd on behalf of Acta Materialia Inc.

This is an open access article under the CC BY license (<http://creativecommons.org/licenses/by/4.0/>)

## 1. Introduction

Micro-alloyed steels containing nanometer-sized precipitates in a ferrite matrix have recently attracted a lot of interest due to their high performance when being used in lightweight automotive parts [1–4]. The combination of high strength, due to the presence of the precipitates, and ductility, originating from the ferritic

matrix, makes their use promising in automotive applications, as these materials substantially reduce energy consumption and consequently CO<sub>2</sub> emission levels.

Vanadium carbide precipitates cause precipitation strengthening of steels [2,5,6]. Therefore, several studies have been focused on the microstructure and mechanical behavior of various steels that contain such precipitates and have undergone different treatments [5,7–10]. Vanadium carbide precipitation takes place either during the austenite to ferrite phase transformation at the migrating austenite/ferrite interface, or in the ferrite phase. The former is called interphase precipitation. The vanadium and carbon solubility is high in austenite but low in the ferrite phase, and their solubility drop when austenite transforms to ferrite drives the interphase precipitation [6]. Understanding the vanadium carbide precipitation and its interaction with the austenite to ferrite phase trans-

\* Corresponding authors.

E-mail addresses: [c.ioannidou@tudelft.nl](mailto:c.ioannidou@tudelft.nl) (C. Ioannidou), [s.e.offerman@tudelft.nl](mailto:s.e.offerman@tudelft.nl) (S.E. Offerman).

<sup>1</sup> Present address: Department of Materials Science and Engineering, KTH Royal Institute of Technology, Brinellvägen 23, Stockholm SE-100 44, Sweden.

<sup>2</sup> Present address: Max-Planck-Institut für Eisenforschung GmbH, Max-Planck-Straße 1, Düsseldorf 40237, Germany.

formation are key factors for achieving an optimum performance of lightweight steels, while minimizing the use of vanadium as alloying element.

The steel composition and the applied thermal treatment determine the vanadium carbide precipitation features. At a temperature range from 600 to 700 °C, the composition of the vanadium carbides can be VC, VC<sub>0.9</sub>, V<sub>4</sub>C<sub>3</sub>, V<sub>6</sub>C<sub>5</sub> [5,7,10–13], while the precipitates may also contain iron (Fe) [14] or manganese (Mn) [15]. These vanadium carbides have been observed as spheres, ellipsoids, disks, rods, needles or cuboids [7–12,16–18]. Their nucleation is favorable at non-KS (Kurdjumov-Sachs) ferrite/austenite interfaces [19,20], while they mainly have a Baker-Nutting orientation relation to the ferritic matrix [5].

Transmission Electron Microscopy (TEM), Atom Probe Tomography (APT) and several spectroscopy techniques have been used to characterize the precipitates [8–10,12–16,18–23]. Nevertheless, the results obtained by these techniques have to be complemented by other types of measurements in order to obtain more accurate statistical information. Moreover, TEM and APT cannot be used to follow the precipitation kinetics *in-situ* during an applied heat treatment. These limitations can be overcome by Small-angle neutron scattering (SANS), which is a non-destructive technique for quantitative precipitation characterization in steels, allowing *in-situ* analysis and providing information from a more statistically representative volume. However, a quantitative analysis of the SANS data requires input from other techniques such as TEM and APT, which can thus complement the SANS measurements.

Interphase precipitation during the austenite to ferrite phase transformation has been studied by *ex-situ* SANS at room temperature in previously heat-treated vanadium micro-alloyed steels, while TEM and APT have been used to reveal the precipitate shape, size and chemical composition, supporting the SANS data analysis [10,16,17]. In these *ex-situ* SANS experiments, the precipitate evolution during the austenite to ferrite phase transformation is measured using a series of samples that have been annealed for different holding times followed by rapid cooling to room temperature. Therefore, these samples consist of complex microstructures with different ferrite, martensite and precipitate fractions. Consequently, it is challenging to accurately separate the precipitate signal from the strong signal arising from the dislocations of the martensite [16].

In the present study we chose to perform *in-situ* SANS measurements in steels as this approach offers the following major advantages. (a) The precipitation kinetics can be measured real-time. (b) The SANS signal from the dislocations in the martensite is avoided since martensite is not present at the high annealing temperatures (>higher than 600 °C). As a result, the SANS signal from the precipitates can be more easily isolated. (c) A SANS background signal can be determined, i.e. a SANS signal from a steel matrix without the presence of precipitates. This background signal can be obtained when measuring at the soaking temperatures that are normally applied in this kind of steels before the isothermal annealing treatments. The soaking temperatures are chosen to be higher than the precipitate dissolution temperatures to assure the absence of any precipitates. The advantages of *in-situ* SANS are manifold and in a recent study we employed the most of them by monitoring the evolution of the precipitate composition in vanadium micro-alloyed steels during annealing at either 650 or 700 °C [14].

The precipitation is closely related to the austenite to ferrite phase transformation and the investigation of the interplay between these two phenomena requires measuring the phase transformation kinetics together with the precipitation kinetics. This can be achieved by combining *in-situ* SANS with neutron diffraction (ND), which can be used for phase identification and quantification. As will be discussed in the following, the combination of *in-situ* SANS and ND offers several advantages over other types of

**Table 1**  
Chemical composition of the investigated steels in wt.% and at.% with balance Fe.

| Steel |      | C     | Mn   | V    | Si    | P      | Cr    | Al    |
|-------|------|-------|------|------|-------|--------|-------|-------|
| LCLV  | wt.% | 0.071 | 1.84 | 0.29 | 0.010 | 0.0010 | 0.010 | 0.004 |
|       | at.% | 0.330 | 1.86 | 0.32 | 0.026 | 0.0018 | 0.011 | 0.008 |
| LCHV  | wt.% | 0.075 | 1.83 | 0.57 | 0.014 | 0.0010 | 0.006 | 0.006 |
|       | at.% | 0.350 | 1.85 | 0.62 | 0.028 | 0.0018 | 0.011 | 0.012 |
| HCHV  | wt.% | 0.140 | 1.83 | 0.57 | 0.013 | 0.0010 | 0.007 | 0.008 |
|       | at.% | 0.620 | 1.85 | 0.62 | 0.026 | 0.0018 | 0.007 | 0.002 |

measurements of phase transformation and precipitation. Nevertheless, such a combination has not been reported in the literature so far and in this respect our study sets the direction for future investigations.

In the present study, *in-situ* and simultaneous ND and SANS measurements are performed in steel samples, which are being heat treated in a furnace. The aim of our study is to provide real-time quantitative information on the interplay between austenite to ferrite phase transformation and the vanadium carbide precipitation kinetics in low-carbon steels. These steels have different vanadium and carbon contents and have been heat treated at different isothermal annealing temperatures (650 or 700 °C). The effects of the annealing temperature and the different vanadium and carbon additions to the steel composition on the phase transformation and precipitation kinetics are investigated. TEM is used to support the SANS data analysis by providing information on the precipitate size and shape.

During the SANS measurements, an external magnetic field of 1.5 T is applied in order to magnetically saturate the steel specimens. In this way we suppress the magnetic-domain scattering, which allows for a quantitative analysis of the precipitation kinetics. The ND measurements show that this external magnetic field affects the phase transformation kinetics. We thus deduce that the magnetic field would eventually also affect the precipitation kinetics. These observations are supported by *in-situ* magnetometer measurements, which also reveal a modification of the austenite to ferrite phase transformation kinetics when an external magnetic field is applied.

Based on the experimental findings, first the phase transformation kinetics in the different steels is analyzed, and the delay in the transformation kinetics due to the external magnetic field is presented. Next, the precipitation kinetics is quantified and finally the coupling between phase transformation and precipitation kinetics is explained.

## 2. Experimental

The phase-transformation and precipitation kinetics are studied in three vanadium micro-alloyed steels with different vanadium and carbon contents. The model alloys were provided by Tata Steel in Europe and their chemical composition is given in Table 1. We refer to these steels as LCLV (low carbon - low vanadium alloy), LCHV (low carbon - high vanadium alloy) and HCHV (high carbon - high vanadium alloy). The high vanadium alloys have twice the concentration of vanadium of the low vanadium one and the high carbon alloy has twice the concentration of carbon compared to the low carbon ones. The atomic ratio of vanadium to carbon is close to 1 in the LCLV and HCHV steels and close to 2 in the LCHV alloy. The manganese concentration is the same in all alloys and the concentration of the other elements is as low as possible. The choice of these steel compositions aims to elucidate and disentangle the effects of vanadium and carbon on the phase transformation and the precipitation kinetics.

The steel alloys were provided as 3 mm thick hot-rolled plates. I-shaped specimens were machined from the center of the plates

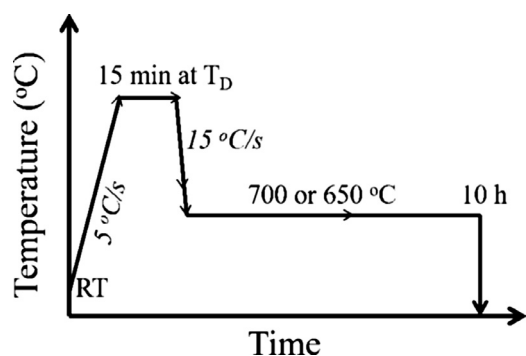


Fig. 1. Thermal cycles applied during the *in-situ* simultaneous ND and SANS measurements.

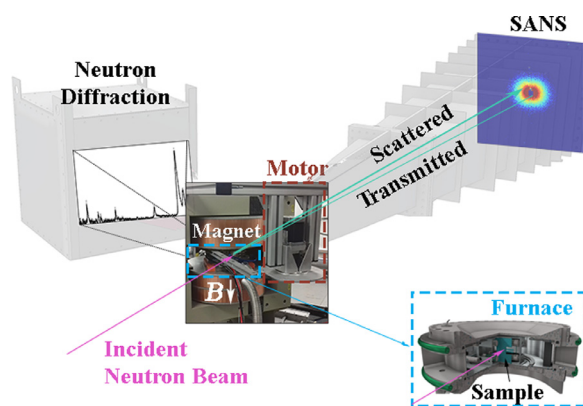


Fig. 2. Experimental set up of the *in-situ* simultaneous ND and SANS.

and are 1 mm thick. The specimen dimensions are chosen so that they fit in a furnace [24] employed for applying the heat treatments to the specimens during the *in-situ* ND and SANS measurements. This furnace uses radiation heating from molybdenum-lanthanum wires and helium gas for cooling. K-type thermocouples are used for temperature control of the specimens.

The thermal cycles followed during the *in-situ* and simultaneous ND and SANS measurements are shown in Fig. 1. The steels are heated up to  $T_D = 1050$  °C (for LCLV specimens) or 1100 °C (for LCHV and HCHV specimens) with a rate of 5 °C/s and held at this temperature for 15 min. These temperatures are  $\sim 50$  °C higher than the precipitate dissolution temperatures of each steel according to ThermoCalc [25] calculations (see Table 5). At these temperatures the steels are fully austenitic and all elements are in solid solution. The specimens are afterwards cooled to 650 or 700 °C with a cooling rate of about 15 °C/s. The austenite to ferrite phase transformation and precipitation are followed during a 10 h isothermal annealing treatment at these temperatures. Finally, the samples are cooled to room temperature.

The *in-situ* and simultaneous ND and SANS measurements are performed at the Larmor Instrument [26] at the ISIS Neutron and Muon Source, STFC Rutherford Appleton Laboratory, UK [27]. The experimental set up is schematically shown in Fig. 2. The furnace operates between the pole shoes of a 3473–70 GMW magnet, which is used to generate a vertical magnetic field of 1.5 T (strong enough to magnetically saturate the specimens) perpendicular to the neutron beam. The furnace is rotating around its vertical axis in order to minimize possible texture effects induced by the materials history, i.e., from the hot-rolling process.

All contributions to the signal that do not come from the sample are subtracted from the data. These contributions are determined through additional ND and SANS measurements performed with an empty furnace (without sample but including all other

parts, e.g. heat shields, etc.) at room temperature while rotating it. The SANS data is normalised to absolute units using the scattering from a reference polymer sample which is a solid blend of hydrogenous and perdeuterated polystyrene. The ND as well as the SANS raw data reduction is performed using the Mantid framework [28].

The size of the incident neutron beam is  $8 \times 8$  mm<sup>2</sup> and the wavelength range for the SANS measurements is 0.42–1.33 nm. The SANS detector is a  $600 \times 600$  mm<sup>2</sup> <sup>3</sup>He tube array with an  $8 \times 8$  mm<sup>2</sup> pixel size, located at 4.3 m from the sample. The scintillator ND detector [29] consists of 128 pixels and is placed on one side of the sample at a distance of 1.15 m from the sample. The ND detector measures *D*-spacing values from 0.07 to 0.3 nm over a diffraction angle range from 49.5 to 76.5 °, which corresponds to a wavelength range from 0.11 to 0.58 nm. Further information on the sample environment and the equipment is given in Ref. [24].

The event-mode data acquisition of the Larmor instrument records both ND and SANS scattering events. Using this mode, each neutron event that is detected has its own time stamp. This allows the re-binning of the data over preferred time slices to be determined after the measurements. Long-time slices provide better statistics and short-time slices a higher temporal resolution of the measured phenomena. Due to the fact that the first hour is more critical for the phase transformation kinetics, 1 min consecutive time slices are chosen during the first hour of annealing and, 5 min time slices every 30 min of measurement time for annealing times longer than 1 h for the ND data ordering. For SANS, 5 min consecutive time slices are chosen during the first hour of annealing and 30 min consecutive time slices for annealing times longer than 1 h.

TEM is used to support the SANS data analysis as it provides complementary information on the precipitate size and shape. The specimens for TEM are heat treated in a DIL-805 A/D dilatometer using inductive heating under a pressure of  $10^{-2}$  mbar and cooling by helium gas. They have rectangular shapes with dimensions  $14 \times 10 \times 1$  mm<sup>3</sup>. The same thermal cycles as the ones shown in Fig. 1 are applied for all three TEM steels, with the temperature controlled by an S-type thermocouple spot-welded in the center of the specimen. Samples of all steels have undergone another heat treatment consisting of heating them up to the soaking temperature,  $T_D$ , and then directly quenching them to room temperature. These samples are used to determine the prior austenite grain size (PAGS).

A JEOL 2010 Transmission Electron Microscope with an accelerating voltage of 200 kV is used for the TEM investigations. Thin foils were prepared for the TEM analysis. 3 mm diameter discs were first extracted from the annealed samples and then ground to 80  $\mu$ m thickness using a Gatan disc grinder. Electrochemical polishing was performed in a solution of 5% perchloric acid (HClO<sub>4</sub>) and 95% acetic acid at 15 °C and a voltage of 25 V with Struers Tunepol 3.

As mentioned above, we have found that the magnetic field applied during the *in-situ* SANS and ND measurements affects the austenite to ferrite phase transformation kinetics. This effect is prominent when comparing the phase-transformation kinetics observed by dilatometry and neutron diffraction. This effect is further investigated by *in-situ* magnetization measurements during isothermal annealing treatments, using a 7307 vibrating sample magnetometer calibrated with a National Institute of Standards and Technology (NIST) nickel specimen. The samples have a rectangular parallelepiped shape of  $2 \times 2 \times 1$  mm<sup>3</sup> (mass 54.8 mg) and are machined from the center of heat-treated dilatometry specimens. A custom made furnace, that can heat the samples up to  $\sim 900$  °C, is used to apply the required heat-treatments and is placed between the poles of the magnet. The magnetization curves are ob-

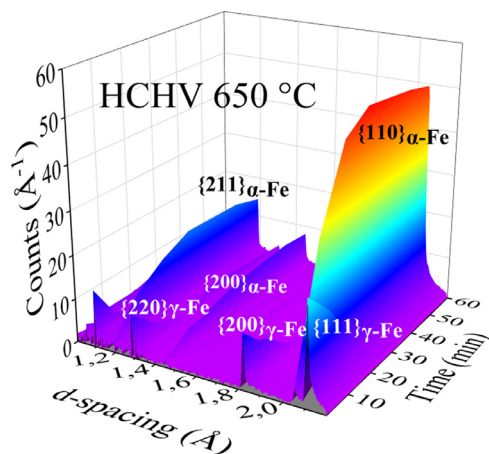


**Fig. 3.** Time evolution of the diffraction peaks of  $\alpha$ -Fe and  $\gamma$ -Fe during the first hour of isothermal annealing of the HCHV steel at 650 °C. The most intense peaks are marked.

tained during a similar thermal cycle under a magnetic field of 1.6 T.

### 3. Phase transformation kinetics

#### 3.a. Neutron diffraction data analysis

Neutron diffraction patterns obtained during the thermal cycle allow for a quantitative analysis of the phase-transformation kinetics during the isothermal annealing stage of the thermal treatment.

During cooling from the soaking temperature to the isothermal annealing temperature, thus before the isothermal holding, the ND patterns do not show any indication of phase transformation. Our quantitative analysis of the phase transformation during the isothermal holding focuses on the time evolution of the ND peak positions and intensities. The peak positions allow the identification of the existent phases while the relative peak intensities (area under the diffraction peaks) are used to determine the fraction of each phase at a specific moment of the annealing (duration of time slice). An example of the time evolution of the diffraction peaks of  $\alpha$ -Fe (ferrite) and  $\gamma$ -Fe (austenite) during the first hour of isothermal annealing of the HCHV steel at 650 °C is presented in Fig. 3. During annealing, austenite is transforming to ferrite since the peak area of the austenitic peaks is decreasing while the area below the ferrite peaks is increasing. All plots that illustrate the time evolution of the ferrite ( $\alpha$ -Fe) and austenite ( $\gamma$ -Fe) diffraction peaks in the LCLV, LCHV and HCHV steels annealed at 650 and 700 °C are provided in the supplementary material (Fig. S2).

In order to obtain the peak areas and positions, we fit the ND peaks using a back-to-back exponential function, which it is the most appropriate function for the analysis of time-of-flight diffraction data [30], and accounts for the non-symmetric peak shape arising from pulse shape of ISIS' second target station. The function is calibrated using Si and NaCaAlF standards. In total five ferritic and three austenitic peaks are fitted. Other peaks, such as the austenitic peaks of {311} and {222} families, are excluded from the calculations because their intensities are very low and comparable to the background. Fig. 4 shows, as an example, the resulting peak fitting of the diffraction peaks of the LCLV sample during the first minute of annealing at 650 °C, after subtraction of the background. The red line is the fitting result and the experimental points are shown in black.

Fitting this model yields the peak area and position ( $D$ -spacing where the peak intensity is maximum) of the eight peaks of interest for each pattern (each time-slice). By applying this fitting

during the entire annealing time, the evolution of the peak area of all peaks is obtained. The area of each ferritic peak is afterwards normalised to the maximum area of this particular peak (obtained for each ferrite peak after phase transformation completion). The peak area of each austenitic peak is also normalised to its maximum (obtained in the beginning of the isothermal annealing). Fig. 5 shows the time evolution of the normalized peak intensities for 5 peaks in the LCLV steel annealed at 650 °C. The data are rather noisy due to counting statistics. Nevertheless, the trend of the peak area evolution with time is the same in all steels, which brings us to the conclusion that the specific texture in the samples does not affect the derived transformed fraction.

For the final calculation of the phase fraction of ferrite formed during each individual time-slice, the weighted average of the area fraction evolution of the normalised ferrite and 1-(normalized austenite) (Fig. 5) peak areas is calculated.

The lattice parameters of austenite and ferrite at 650 and 700 °C are obtained from the positions of the diffraction peaks corresponding to each phase. The lattice parameter of each phase at a certain temperature is the average value of the lattice parameters calculated from the positions of the measured peaks of this phase, averaged also over the annealing period that this phase is present. The resulting austenite lattice parameter is  $a_{\gamma\text{-Fe}} = 0.364 \pm 0.006$  nm and the ferrite lattice parameter is  $a_{\alpha\text{-Fe}} = 0.290 \pm 0.001$  nm. The effect of temperature on the lattice parameter of each phase is not detected since the 2 temperatures are very close.

#### 3.b. Neutron diffraction results and discussion

The phase transformation kinetics derived from the neutron diffraction data analysis of the LCLV, LCHV and HCHV steels at the two annealing temperatures of 650–700 °C is presented in Fig. 6a and b. The graphs in Fig. 6c and d depict enlarged parts of the plots of Fig. 6a and b, respectively, showing the phase-transformation kinetics during the first hour of annealing. Austenite to ferrite phase transformation takes place in all steels at both temperatures since the isothermal annealing temperature is lower than the  $A_3$  temperature of these steels (Table 3). In all cases, the phase transformation is completed during the 10 h annealing treatment.

According to the Kolmogorov-Johnson-Mehl-Avrami (KJMA) equation [31], the transformed phase fraction  $f$  as a function of annealing time  $t$  is given by:

$$f(t) = 1 - \exp(-A \cdot t^n), \quad (1)$$

with  $A$  the rate constant, which contains information on the nucleation and growth characteristics, and  $n$  the Avrami exponent. Cahn et al. [32] report that for site-saturated phase transformations on grain surfaces  $n = 1$  and Eq. (1) can be written as:

$$f(t) = 1 - \exp(-A \cdot t), \quad (2)$$

where  $A = 2 \cdot B \cdot v$ , with  $B$  the grain surface-to-volume ratio (in  $\text{m}^{-1}$ ) and  $v$  a constant growth rate. According to Chen et al. [18], the increase in the ferrite fraction,  $f_{\alpha}$ , can be calculated from the relation:

$$df_{\alpha} = \frac{v_{\alpha\gamma}}{d_{\gamma}} dt \Rightarrow v_{\alpha\gamma} = \frac{df_{\alpha}}{dt} d_{\gamma}, \quad (3)$$

where  $v_{\alpha\gamma}$  is the overall austenite/ferrite interface velocity and  $d_{\gamma}$  is half the prior austenite grain size.

In order to quantify and understand the phase-transformation kinetics of the three alloys during annealing at 650 and 700 °C, the phase transformation curves plotted in Fig. 6c and d are fitted to Eq. (2). The fits are performed on the data of the first 10 or 20 min of the isothermal annealing, depending on the steel composition and annealing temperature, because this is the period during which more than half of the austenite is transformed to ferrite

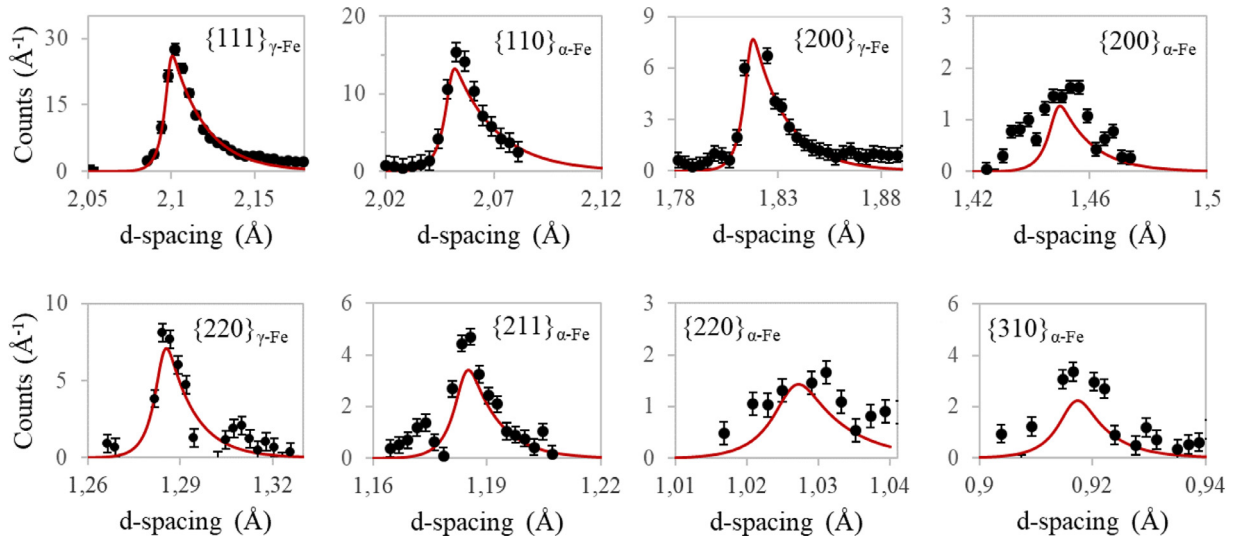


Fig. 4. Peak fitting of the diffraction peaks, yielding both their position and intensity, of the LCLV steel during the 1st minute of annealing at 650 °C.

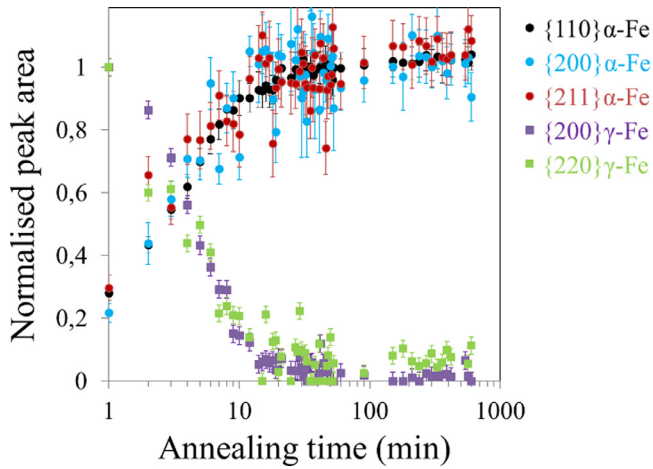


Fig. 5. Time evolution of the normalized peak intensity area for 3 ferritic and 5 austenitic peaks for the LCLV steel annealed at 650 °C.

(see Fig. 6c and d). The quality of the fits is highlighted by the agreement between the (fitted) solid lines and the experimental data points shown in Fig. 6c and d. For these fits, we use  $n = 1$ , a value which is consistent with the data and indicates that all samples undergo a site-saturated phase transformation on grain surfaces with a constant growth rate [32]. This fitting procedure thus leads to the determination of the  $A$  value for each sample. The interface velocity  $v_{\alpha\gamma}$  which reflects the speed of the austenite to ferrite phase transformation is calculated from Eq. (3) as the product of the  $A$  value with the half of the prior austenite grain size,  $d_\gamma$ .  $d_\gamma$  is experimentally measured from the dilatometry treated samples heated up to the soaking temperature and directly quenched to room temperature. The results are summarized in Table 2.

In an attempt to understand the phase-transformation kinetics in the three steels at 650 and 700 °C, in the following we consider resolving the combined effects of vanadium and carbon as well as the effect of the precipitates on the velocity of the austenite/ferrite interface,  $v_{\alpha\gamma}$ .  $v_{\alpha\gamma}$  is described by the equation [33]:

$$v_{\alpha\gamma} = M \cdot \Delta G_{\text{net}}, \quad (4)$$

where  $\Delta G_{\text{net}}$  is the total driving force for the phase transformation and  $M$  is the intrinsic mobility of the interface without taking into account the solute drag effect. The interface mobility is expressed

as [34]:

$$M = M_0 \cdot \exp\left(-\frac{Q_0}{RT}\right), \quad (5)$$

where  $M_0$  is a pre-exponential factor,  $Q_0$  is the activation energy for the transfer of atoms across the interface and  $R$  is the gas constant ( $8.31 \text{ J mol}^{-1} \text{ K}^{-1}$ ).

The total driving force for the phase transformation,  $\Delta G_{\text{net}}$ , is the chemical driving force for phase transformation in the beginning of annealing reduced by the dissipation of Gibbs energy caused (a) by the diffusion of the solute atoms, i.e. vanadium, carbon and manganese, being dragged along with the migrating interface:  $\Delta G_{\text{diss}}^V$ ,  $\Delta G_{\text{diss}}^C$  and  $\Delta G_{\text{diss}}^{\text{Mn}}$ , respectively, and (b) by the Zener pinning force,  $P_z$ , caused by the precipitates. The net difference in Gibbs free energy available to drive the  $\gamma/\alpha$  interface against the interface friction is:

$$\Delta G_{\text{net}} = \Delta G_{\text{chem}} - \Delta G_{\text{diss}}^V - \Delta G_{\text{diss}}^C - \Delta G_{\text{diss}}^{\text{Mn}} - P_z. \quad (6)$$

$\Delta G_{\text{chem}}$  is obtained for each steel at a certain temperature using the ThermoCalc software. Furthermore, the precipitate Zener pinning force can be calculated from [35]:

$$P_z = \frac{3 \cdot f_V \cdot \gamma_p}{d_p}, \quad (7)$$

where  $f_V$  is the volume fraction of precipitates,  $d_p$  is the diameter of the precipitates and  $\gamma_p$  is the interface energy between the precipitates and their matrix (taken as  $0.5 \text{ J/m}^2$  here [36]). Combining Eqs. (4) and (6) leads to:

$$v_{\alpha\gamma} = M \cdot (\Delta G_{\text{chem}} - \Delta G_{\text{diss}}^V - \Delta G_{\text{diss}}^C - \Delta G_{\text{diss}}^{\text{Mn}} - P_z). \quad (8)$$

According to the Hillert–Sundman dissipation model, the Gibbs energy dissipation or the solute drag force is [37,38]:

$$\Delta G_{\text{diss}} = -\frac{V_M}{\dot{S}} \int_{-\delta}^{\delta} J \cdot \frac{d\mu}{ds} ds. \quad (9)$$

In Eq. (9),  $\dot{S}$  is the growth rate (being equal to  $v_{\alpha\gamma}$  in our case),  $V_M$  is the molar volume,  $\mu$  is the chemical potential of a solute in the  $\alpha/\gamma$  interphase boundary region given by:

$$\mu = R \cdot T \cdot \left( \ln x + \sum_j \varepsilon_j x \right) + E + \Delta E \cdot \left( 1 + \frac{S}{\delta} \right), \quad (10)$$

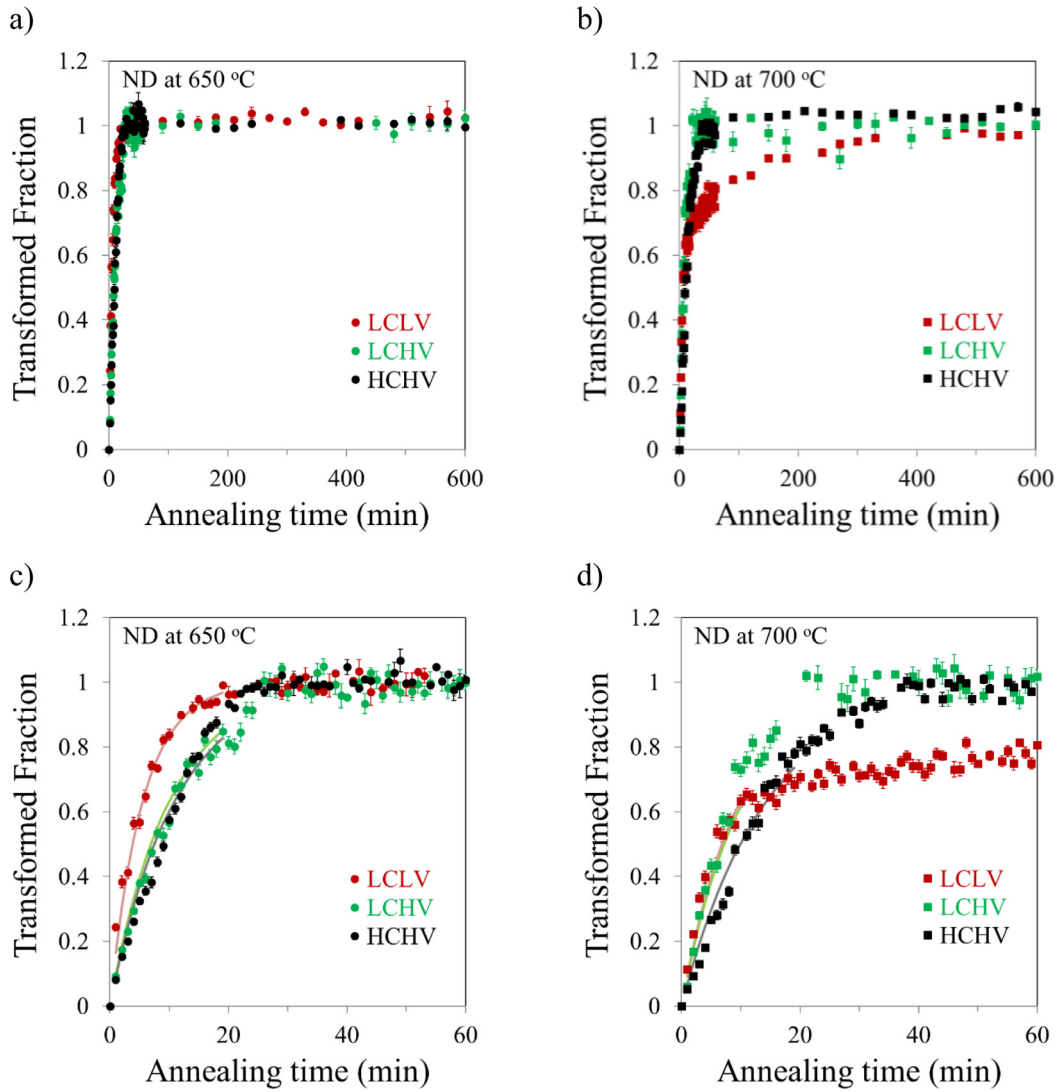


**Fig. 6.** Time evolution of the transformed austenite fraction in the LCLV, LCHV and HCHV steels at the two annealing temperatures of (a) 650 °C and (b) 700 °C. The graphs in Fig. c and d are enlarged parts of the plots of Fig. a and b, respectively, showing the phase transformation kinetics during the first hour of annealing. The solid lines in each curve are the fits of the phase transformation kinetics during the first minutes of annealing with Eq. (1).

**Table 2**

The parameter,  $A$ , of the phase transformation curves and the obtained austenite/ferrite interface velocity,  $v_{\alpha\gamma}$ , for the three steels at two annealing temperatures, obtained by the fits of the *in-situ* ND patterns.

|      | AnnealingT ( °C) | $A(\text{min}^{-1})$ | PAGS( $\mu\text{m}$ ) | $d_{\gamma}(\mu\text{m})$ | $v_{\alpha\gamma}(\mu\text{m/s})$ |
|------|------------------|----------------------|-----------------------|---------------------------|-----------------------------------|
| LCLV | 650              | $0.114 \pm 0.013$    | $63 \pm 3$            | $31.5 \pm 1.5$            | $0.060 \pm 0.007$                 |
|      | 700              | $0.101 \pm 0.012$    | $63 \pm 3$            | $31.5 \pm 1.5$            | $0.053 \pm 0.007$                 |
| LCHV | 650              | $0.096 \pm 0.002$    | $66 \pm 2$            | $33 \pm 1$                | $0.053 \pm 0.002$                 |
|      | 700              | $0.096 \pm 0.011$    | $66 \pm 2$            | $33 \pm 1$                | $0.053 \pm 0.006$                 |
| HCHV | 650              | $0.090 \pm 0.008$    | $62 \pm 2$            | $31 \pm 1$                | $0.047 \pm 0.005$                 |
|      | 700              | $0.070 \pm 0.002$    | $62 \pm 2$            | $31 \pm 1$                | $0.036 \pm 0.001$                 |

and  $J$  is the diffusion flux of a solute through the interface:

$$J = \frac{D^b \cdot x}{R \cdot T} \cdot \frac{\partial \mu}{\partial s} \quad (11)$$

In Eqs. (9)–(11),  $x$  is the solute concentration,  $\delta$  is half the thickness of the boundary,  $s$  is a coordinate taking values in the range  $[-\delta, \delta]$ ,  $E$  is the interaction potential of the solute to the  $\alpha/\gamma$  interface,  $\Delta E$  is half the difference in the free energy of solute between ferrite and austenite,  $\varepsilon_j$  is the Wagner's parameter reflecting the interaction of the solute with the other  $j$  solutes, and  $D^b$  is the dif-

fusion coefficient of a solute inside the interphase boundary (taken constant inside the boundary).

Using Eqs. (10) and (11), Eq. (9) can be finally written as:

$$\Delta G_{\text{diss}} = -\frac{V_M}{v_{\alpha\gamma}} \cdot \frac{D^b \cdot x}{R \cdot T} \cdot \frac{\Delta E^2}{\delta} \cdot 2 = C \frac{x}{v_{\alpha\gamma}}, \quad (12)$$

where  $C = -2 \cdot \frac{V_M \cdot D^b \cdot \Delta E^2}{R \cdot T \cdot \delta}$ , and its value is different for each element, in our case, vanadium,  $C^V$ , carbon,  $C^C$ , or manganese,  $C^{\text{Mn}}$ , since  $D^b$  and  $\Delta E$  are different for the three elements.

**Table 3**

List of parameters calculated for the alloys of interest. The  $A_3$  temperature and the  $\Delta G_{\text{chem}}$  are calculated by ThermoCalc. The  $\Delta G_{\text{diss}}^{\text{V}}$ , the  $\Delta G_{\text{diss}}^{\text{Mn}}$ , the  $P_z$  and the  $\Delta G_{\text{net}}$  are obtained by solving the set of equations as explained in text.

| Steel | AnnealingT (°C) | $A_3$ (°C) | $\Delta G_{\text{chem}}$ (J/mol) | $\Delta G_{\text{diss}}^{\text{V}}$ (J/mol) | $\Delta G_{\text{diss}}^{\text{Mn}}$ (J/mol) | $P_z$ (J/mol) | $\Delta G_{\text{net}}$ (J/mol) |
|-------|-----------------|------------|----------------------------------|---|--|---------------|---------------------------------|
| LCLV  | 650             | 830        | 435                              | 53 ± 10                                     | 7 ± 21                                       | 3             | 372 ± 23                        |
|       | 700             | 830        | 241                              | 20 ± 10                                     | 34 ± 13                                      | 2             | 185 ± 16                        |
| LCHV  | 650             | 853        | 457                              | 117 ± 25                                    | 8 ± 24                                       | 4             | 328 ± 35                        |
|       | 700             | 853        | 262                              | 40 ± 11                                     | 34 ± 12                                      | 3             | 185 ± 16                        |
| HCHV  | 650             | 834        | 435                              | 131 ± 25                                    | 9 ± 27                                       | 3             | 292 ± 37                        |
|       | 700             | 834        | 239                              | 58 ± 14                                     | 50 ± 18                                      | 4             | 127 ± 23                        |

Based on the above, Eq. (8) can be rewritten as:

$$v_{\alpha\gamma} = M \cdot \left( \Delta G_{\text{chem}} - C^{\text{V}} \cdot \frac{x^{\text{V}}}{v_{\alpha\gamma}} - C^{\text{C}} \cdot \frac{x^{\text{C}}}{v_{\alpha\gamma}} - C^{\text{Mn}} \cdot \frac{x^{\text{Mn}}}{v_{\alpha\gamma}} - \frac{3 \cdot f_{\text{V}} \cdot \gamma_{\text{p}}}{d_{\text{p}}} \right). \quad (13)$$

The Gibbs energy dissipation as a result of the manganese spike in front of the  $\gamma/\alpha$  interface is neglected in these calculations, since the work of Chen et al. [39] shows that this contribution is minor when the interface velocity is of the order of  $10^{-7}$  m/s. The latter study refers to the isothermal bainitic ferrite formation at 550 °C and we assume similar trends at 650 and 700 °C, however, this should be further investigated in the future. The Gibbs energy dissipation due to the vanadium spike is also neglected here, according to Refs. [15,40]. The precipitate volume fraction and size that are necessary for the Zener pinning force calculation are obtained experimentally from the quantitative SANS data analysis described later in this paper. Possible energy dissipation due to the presence of curved boundaries that cause pressure increase is considered to be negligibly small as in Ref. [41].

We use Eq. (13) to analyze the behavior of the LCLV, LCHV, and HCHV steels at each annealing temperature, 650 and 700 °C. By solving the set of the equations, we obtain the  $C^{\text{V}}$ ,  $C^{\text{C}}$  and  $C^{\text{Mn}}$  values and eventually calculate the  $\Delta G_{\text{diss}}^{\text{V}}$ ,  $\Delta G_{\text{diss}}^{\text{C}}$  and  $\Delta G_{\text{diss}}^{\text{Mn}}$ . The results show that the Gibbs energy dissipation due to carbon segregation at  $\alpha/\gamma$  interfaces,  $\Delta G_{\text{diss}}^{\text{C}}$ , is close to zero and can therefore be neglected.  $\Delta G_{\text{diss}}^{\text{C}}$  is considered to be zero in other studies as well, as for example in Ref. [41]. However, despite the negligible  $\Delta G_{\text{diss}}^{\text{C}}$ , carbon may have an indirect effect on the total Gibbs energy dissipation through its participation in the precipitation.

The derived  $\Delta G_{\text{diss}}^{\text{V}}$ ,  $\Delta G_{\text{diss}}^{\text{Mn}}$  and  $P_z$  and the resulting  $\Delta G_{\text{net}}$  for the LCLV, LCHV and HCHV steels at 650 and 700 °C annealing temperatures are summarized in Table 3. The errors in the  $\Delta G_{\text{diss}}^{\text{V}}$  and  $\Delta G_{\text{diss}}^{\text{Mn}}$  are based on the uncertainties (~5%) introduced by the calculation of the interface velocities.

The intrinsic mobility of the interface is calculated from the fit of the experimental data using Eq. (13) and it is for each annealing temperature:  $M_{650} = 1.5 \times 10^{-10}$  m mol  $\text{J}^{-1}$   $\text{s}^{-1}$  at 650 °C and  $M_{700} = 2.9 \times 10^{-10}$  m mol  $\text{J}^{-1}$   $\text{s}^{-1}$  at 700 °C.

The activation energy for the transfer of atoms across the interface,  $Q_0$ , can also be obtained using Eq. (8) and it is found to amount to 90 kJ/mol. Ideally, *in-situ* measurements during the austenite to ferrite phase transformation in pure iron should be performed in order to determine it. A value of 140 kJ/mol for  $Q_0$  is often mentioned in the literature [42], reported by Krielaart and van der Zwaag [34]. Hillert [37] reported a similar value,  $Q_0 = 144$  kJ/mol, but this was experimentally obtained during recrystallization in pure Fe, not during austenite to ferrite phase transformation. Our  $Q_0 = 90$  kJ/mol differs substantially from the literature values. The precipitation that takes place simultaneously to phase transformation as well as the magnetic field that is applied during the measurements significantly affect the mobility, the interface velocity and the energy dissipation, eventually resulting in a different  $Q_0$  value.

The time evolution of the transformed austenite fraction or, in other words, the ferrite fraction evolution during annealing of the LCLV, LCHV and HCHV steels is determined as described in Section 3.a. Fig. 6a shows the results for the annealing temperature of 650 °C and Fig. 6b for 700 °C. Austenite to ferrite phase transformation is observed in all steels at both temperatures and it is completed during the 10 h annealing treatment in all cases. This is in agreement with ThermoCalc calculations which also show that phase transformation takes place in all steels, at both temperatures and that the equilibrium ferrite fraction is larger than 98% in all cases. The phase-transformation kinetics vary depending on the steel composition, i.e. the concentration of vanadium and carbon in each alloy, as well as on the annealing temperature. The kinetics are reflected in the calculated velocities  $v_{\alpha\gamma}$  listed in Table 2.

The derived phase-transformation kinetics curves show that the first hour of annealing, and more specifically the first 20 min, are the most critical for the transformation. In all steels after 20 min more than 80% of austenite has already been transformed at 650 °C, while at 700 °C this fraction is more than 60%. For all alloys, the kinetics is significantly faster at 650 than at 700 °C, which we attribute to the larger driving force for phase transformation at the lower temperature. However, we note that this difference is very small for the LCHV sample.

The comparison of the kinetics observed for the different samples gives insight into the effect of the different concentrations of vanadium and carbon on the rate of phase transformation. At 650 °C, the fastest phase-transformation kinetics is measured for the LCLV steel. The kinetics for the LCHV steel are slower and the HCHV steel has the slowest phase-transformation velocity. After 30 min of annealing the phase transformation has been completed in all steels. At 700 °C, during the first 10 min of annealing, the phase transformation in the LCLV and LCHV steels occurs with the same rate and with a lower rate in the HCHV steel. However, at longer times the transformation in the LCLV steel is not faster than in the other two steels. After 40 min of annealing at 700 °C the phase transformation has been completed in the LCHV and HCHV steels but not in the LCLV alloy in which 10 h are necessary to complete the phase transformation.

Additions of vanadium and carbon to the steel composition cause the retardation of the phase transformation. In each steel, the effect of the element concentrations on the kinetics of phase transformation is explained through the Gibbs energy dissipation as described above. The different element additions determine the dissipation of the Gibbs energy due to each element,  $\Delta G_{\text{diss}}$ , affecting the total driving force for the phase transformation,  $\Delta G_{\text{net}}$ , which together with the mobility control the ferrite growth velocity. The precipitate pinning force has a small effect on the velocity comparing to the effect of energy dissipation.

At both temperatures, 650 and 700 °C,  $\Delta G_{\text{net}}$  is the largest for the alloy with the lowest vanadium and carbon concentration, i.e., for the LCLV. Adding vanadium to the steel causes a systematic decrease in  $\Delta G_{\text{net}}$  (comparison between LCLV and LCHV) and the same trend is observed with the addition of carbon (comparison between LCHV and HCHV), despite the high uncertainty in the cal-



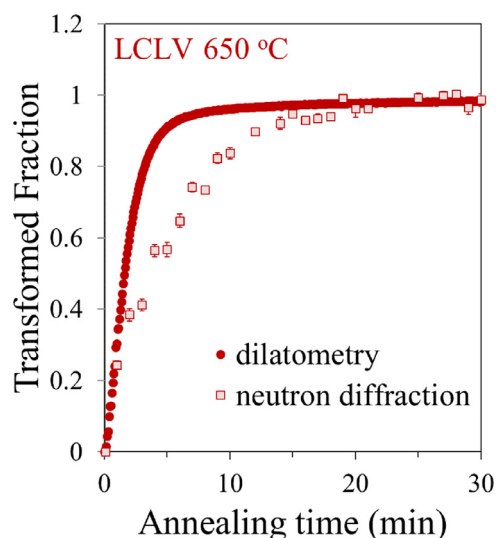


Fig. 7. Transformed austenite fraction measured by ND and dilatometry for the LCLV steel at 650 °C.

culations (reflected in the errors).  $\Delta G_{\text{diss}}$  due to vanadium is increasing either by adding vanadium or carbon to the steel, or by lowering the annealing temperature, while the dissipation due to manganese is not affected by these factors.

For each individual alloy annealed at 700 °C, the energy dissipation due to vanadium is smaller than at 650 °C, while the opposite trend is observed for the manganese dissipation, leading to the conclusion that the temperature effect on the Gibbs energy dissipation can vary between the different elements causing the dissipation. According to Eq. (12), the annealing temperature affects the energy dissipation directly, but also through its effect on  $\Delta E$  and the diffusion coefficient of each solute. The magnetic field applied during the measurements also affects the Gibbs energy dissipation as will be explained in Section 3.c.

### 3.c. Effect of the external magnetic field on the phase transformation kinetics

A delay in the onset and time evolution of austenite to ferrite phase transformation is observed in the results obtained from the ND experiments compared to the ones obtained from the dilatometry heat-treatments applied for the TEM sample preparation. An example is shown in Fig. 7, in which we compare the time evolution of the transformed austenite fraction measured by ND and dilatometry for the LCLV steel at 650 °C. These samples have been submitted to the same heat treatment and the only difference is that a magnetic field of  $\sim 1.5$  T is applied during the ND measurements. In the following we discuss the effect of the external magnetic field on the austenite-to-ferrite phase-transformation kinetics by comparing (zero field) dilatometry with *in-situ* magnetometry under a magnetic field of 1.6 T.

As the furnace used for the magnetometer measurements is not able to reach temperatures higher than 900 °C, we applied a slightly different heat treatment for this set of samples used for dilatometry and magnetometry. For these measurements the samples are first heat treated in the dilatometer at 1050 °C for 10 min and then quenched to room temperature in order to dissolve the precipitates that are initially present at room temperature (Fig. 8a). Afterwards, a heat treatment is applied including holding at 900 °C for 10 min to austenitize the sample, followed by an isothermal holding at 650 °C for 55 min. The phase-transformation kinetics at 650 °C is therefore measured by both techniques individually for each alloy. In order to obtain the phase-transformation kinetics

by magnetometry, the magnetization evolution of the specimen is translated to volume fraction evolution of the ferromagnetic phase, i.e. the ferrite (austenite is paramagnetic). This is done by normalizing the magnetization at each moment of annealing to the maximum magnetization reached after 50 min when the austenite-to-ferrite phase transformation is complete. The time evolution of the magnetization during annealing of the LCLV at 650 °C is provided in the supplementary material (Fig. S3).

The time evolution of the ferrite phase fraction for the LCLV steel obtained during annealing at 650 °C from magnetometry under a magnetic field of 1.6 T is plotted in Fig. 8b, together with the corresponding fraction obtained from the zero field dilatometry measurements. The comparison of the two curves highlights the delay in the phase-transformation kinetics induced by the magnetic field. This delay cannot be explained by the Zeeman energy effect because, according to Ref. [43], when a small magnetic field is applied, the critical temperatures for phase transformation do not significantly change. In addition, these small changes in the critical temperatures due to the magnetic field, would slightly increase the driving force for phase transformation accelerating in this way the phase-transformation kinetics. This is contradictory to our observations. Possible explanations for the observed retardation of the phase-transformation kinetics by the magnetic field might be related to a modification of the carbon diffusivity below and above the Curie temperature due to magnetostriction [44], as well as modification of the grain boundary energy. The magnetization of ferrite above and below the Curie temperature, as well as the magnetization of austenite are critical factors for ferrite nucleation when a magnetic field is applied. In addition, research is required on the effect of the magnetic field on the phase-transformation kinetics in different steels heat treated at different temperatures. The magnetic-field effect may be dependent on the steel composition and the annealing temperature. For example, we observe a delay in the phase-transformation kinetics in the LCLV steel annealed at 700 °C after 10 min of annealing (Fig. 6b), which may be due to the magnetic field. It is important to mention here that the magnetic field may influence the mobility,  $M$ , and the dissipation energy due to different elements which finally affect  $v_{\alpha\gamma}$ , thus it would be interesting if future research could quantify these effects. To conclude, more extensive work is required in order to explain the effect of the magnetic field on the phase-transformation kinetics. Such a study, however is beyond the scope of this paper.

## 4. Precipitation kinetics

### 4.a. SANS data analysis

The time evolution of the SANS intensity during annealing reveals the precipitation kinetics in the studied steels. It is a 2D pattern from which the macroscopic differential scattering cross-section,  $(d\Sigma/d\Omega)(Q)$ , can be obtained after background correction and neutron flux calibration [45].  $(d\Sigma/d\Omega)(Q)$  is a function of the scattering vector,  $Q$ , and has two components, the nuclear,  $(d\Sigma/d\Omega)_{\text{NUC}}(Q)$ , and the magnetic,  $(d\Sigma/d\Omega)_{\text{MAG}}(Q)$ , cross sections. These two components originate from the strong nuclear interaction of the neutrons with the nuclei and from the dipole-dipole interaction of the neutron magnetic moments with the unpaired electrons of the atoms, respectively [46]. Due to the specific selection rules of the magnetic scattering it is possible to unambiguously separate the magnetic contribution from the nuclear contribution to the cross-section, by applying a magnetic field, high enough to saturate the magnetization of the specimen, along a direction contained in the SANS detector plane. In this case, the

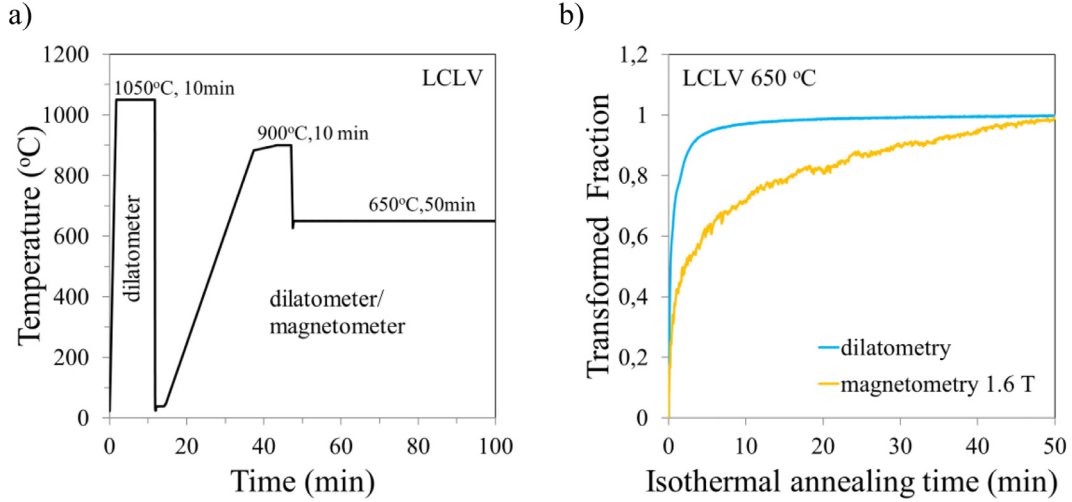


**Fig. 8.** (a) Heat treatment applied to the LCLV steel. (b) Comparison of phase transformation kinetics of the LCLV steel obtained during annealing at 650 °C by dilatometry (at zero magnetic field) and magnetometry (under a magnetic field of 1.6 T).

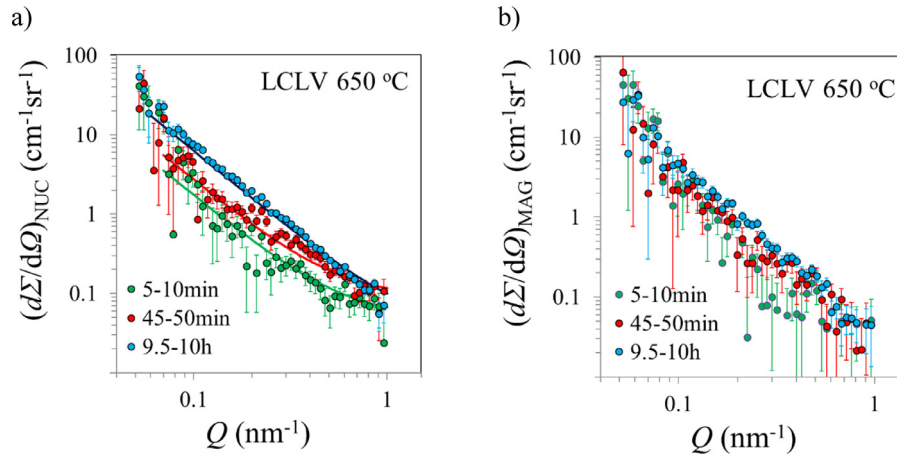


**Fig. 9.** Time evolution of the SANS scattering cross section, corrected for background and dislocation scattering, of the LCLV steel annealed at 650 °C. (a) nuclear scattering; (b) magnetic scattering. The solid lines in (a) are fits with Eq. (15).

macroscopic differential scattering cross-section equals to [46]:

$$\left(\frac{d\Sigma}{d\Omega}\right)(\mathbf{Q}) = \left(\frac{d\Sigma}{d\Omega}\right)_{\text{NUC}}(\mathbf{Q}) + \left(\frac{d\Sigma}{d\Omega}\right)_{\text{MAG}}(\mathbf{Q}) \cdot \sin^2\varphi \quad (14)$$

where  $\varphi$  is the angle between the magnetic field direction and  $\mathbf{Q}$ . In this study we average  $(d\Sigma/d\Omega)(\mathbf{Q})$  azimuthally over sectors of 30 ° around the transmitted neutron beam, oriented parallel and perpendicular to the magnetic field, respectively. In this way we obtain  $(d\Sigma/d\Omega)_{\text{NUC}}(\mathbf{Q})$  and  $(d\Sigma/d\Omega)_{\text{NUC}}(\mathbf{Q}) + (d\Sigma/d\Omega)_{\text{MAG}}(\mathbf{Q})$ , respectively and from the difference between these two values we calculate  $(d\Sigma/d\Omega)_{\text{MAG}}(\mathbf{Q})$ .

The determination of  $(d\Sigma/d\Omega)_{\text{NUC}}(\mathbf{Q})$  requires an accurate background subtraction. Since the SANS measurements are performed on samples being heat treated inside the furnace, the background signal consists of the scattering signal from the furnace and from the steel matrix. The latter is determined from measurements on a reference steel without precipitates, at soaking temperature. Therefore, after background subtraction,  $(d\Sigma/d\Omega)_{\text{NUC}}(\mathbf{Q})$  contains only the scattering from the precipitates.

Examples of the SANS nuclear differential scattering cross sections obtained at different annealing times of the LCLV steel at 650 °C are shown in Fig. 9a. The corresponding magnetic scattering cross sections are shown in Fig. 9b. The SANS cross sections increase with time, as expected for precipitation. More SANS results

obtained during annealing of the LCLV, LCHV and HCHV steels at 650 and 700 °C can be found in the supplementary material (Figs. S4–S6).

$(d\Sigma/d\Omega)_{\text{NUC}}(\mathbf{Q})$  is analyzed in order to obtain quantitative information on the precipitation kinetics, which, for a dilute system of precipitates within a homogeneous matrix, is given by [45]:

$$\left(\frac{d\Sigma}{d\Omega}\right)_{\text{NUC}}(\mathbf{Q}) = \Delta\rho_{\text{NUC}}^2 \cdot \int D_N(r) \cdot V^2(r) \cdot P^2(\mathbf{Q}, r) dr, \quad (15)$$

where  $r$  and  $V$  are the precipitate radius and volume, respectively,  $D_N(r)$  is the size distribution of the particles,  $\Delta\rho_{\text{NUC}}^2$  is the difference in nuclear scattering length density between the matrix and the precipitates (nuclear contrast), and  $P(\mathbf{Q}, r)$  is the orientation-averaged form factor reflecting the precipitate shape. For ellipsoidal precipitates, the form factor is [47]:

$$P(\mathbf{Q}, r) = 3 \frac{\sin(\mathbf{Q}r) - (\mathbf{Q}r) \cos(\mathbf{Q}r)}{(\mathbf{Q}r)^3}, \quad (16)$$

where

$$r = (R_{\text{eq}}^2 \sin^2\psi + R_p^2 \cos^2\psi)^{1/2}. \quad (17)$$

$\psi$  is the angle between the axis of the ellipsoid and the  $\mathbf{Q}$ ,  $R_{\text{eq}}$  is the equatorial radius (radius perpendicular to the rotational axis of the ellipsoid) and  $R_p$  is the polar radius (radius along the rotational

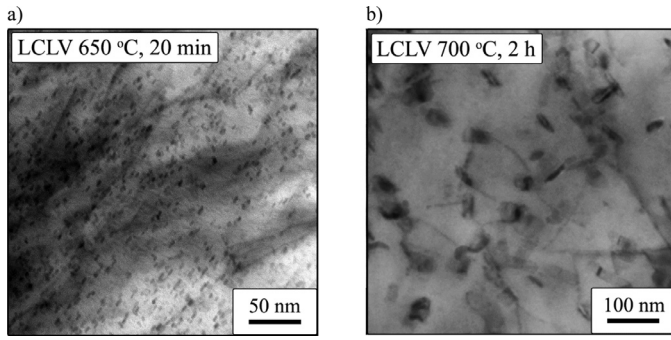


**Fig. 10.** TEM bright field images obtained from thin foils showing the ellipsoidal shape of the precipitates. The micrographs correspond to samples from the LCLV steel annealed at (a) 650 °C for 20 min and (b) at 700 °C for 2 h.

axis of the ellipsoid). In this study, the precipitate is modeled as an oblate ellipsoidal for all steels, based on TEM analysis (see Fig. 10). Fitting trials of the SANS data to model the precipitate shape as spherical were initially performed, but it was found that the spherical model is not able to describe the precipitate shape for all alloys and annealing temperatures. Examples of the precipitate ellipsoidal shape are illustrated in the TEM micrographs of Fig. 10a and b, which correspond to LCLV steel samples annealed at 650 °C and 700 °C, respectively. More TEM micrographs can be found in the supplementary material of this article (Fig. S7). Note here that TEM is used for a qualitative investigation of the precipitate shape in order to contribute to the SANS analysis, and not to obtain quantitative information on the precipitate shape and size. The reason behind this is in the differences in the phase-transformation and precipitation kinetics between the steels heat-treated in the dilatometer without a magnetic field and in the furnace under the effect of an external magnetic field. This is explained in detail later in the text.

Finally, in Eq. (15), the term  $\Delta\rho_{\text{NUC}}^2$  is the nuclear contrast between the precipitates and the matrix. This contrast is composition dependent and can be calculated according to [14]. Therefore,  $\Delta\rho_{\text{NUC}}^2$  is different for the three steels, since the precipitate chemical composition varies with the steel composition and the temperature [14]. In the following we assume that all precipitates in the same steel annealed at the same temperature have the same composition.

In order to obtain quantitative information on the precipitation kinetics from the SANS data, we fit the  $(d\Sigma/d\Omega)_{\text{NUC}}(Q)$  curves to the model of Eq. (15) using the SasView software [48]. For this purpose we assume an oblate ellipsoidal precipitate shape, according to Eqs. (16) and (17), with  $R_{\text{eq}}$  and  $R_{\text{p}}$  of the precipitates following a log-normal distribution. The fitting parameters of the model are the precipitate-size distribution (i.e.,  $R_{\text{eq}}$ ,  $R_{\text{p}}$  and their log-normal distribution) and the precipitate volume fraction,  $f_{\text{V}}$ , for each SANS curve that corresponds to a specific time-slice of annealing. The precipitate number density,  $N_{\text{p}}$ , is eventually calculated from the  $f_{\text{V}}$ ,  $R_{\text{eq}}$  and  $R_{\text{p}}$  values, taking into account the volume of the oblate ellipsoidal:

$$N_{\text{p}} = \frac{f_{\text{V}}}{\frac{4}{3} \cdot \pi \cdot R_{\text{eq}}^2 \cdot R_{\text{p}}} \quad (18)$$

It is important to note that the  $(d\Sigma/d\Omega)_{\text{NUC}}(Q)$  curves measured during cooling from the austenization temperature to the isothermal temperature indicate that no precipitation is taking place before the isothermal annealing temperature is reached. Indeed, the SANS curves captured during cooling (1 min time-slices) and those at the soaking temperature overlap.

In a dual phase system and for small precipitate volume fractions, the precipitate volume fraction is expressed as [46]:

$$f_{\text{V}} \cong \frac{Q_{0,\text{NUC}}}{2\pi^2 \Delta\rho_{\text{NUC}}^2}, \quad (19)$$

where the invariant  $Q_{0,\text{NUC}}$  is the area under the Kratky plot curve,  $Q^2(d\Sigma/d\Omega)_{\text{NUC}}(Q)$  vs  $Q$  plot, given by:

$$Q_{0,\text{NUC}} = \int_0^{\infty} Q^2 \left( \frac{d\Sigma}{d\Omega} \right)_{\text{NUC}}(Q) dQ = 2\pi^2 \Delta\rho_{\text{NUC}}^2 f_{\text{V}}. \quad (20)$$

From Eq. (19), it is clear that the precipitate's chemical composition and consequently  $\Delta\rho_{\text{NUC}}^2$ , determine the resulting precipitate volume fraction values. The determination of the precipitate's chemical composition, size and volume fraction is thus challenging and strongly depends on the concentration gradients around the precipitate.

For precipitates with a vanadium-rich core and an iron-rich shell as considered in Ref. [14] and as shown in Fig. 11, representation I, the precipitate size depends on the size of the iron concentration in the outer part of the precipitate. For short annealing times, the size of the iron-rich shell is large and the size of the vanadium rich core is small, giving a small overall precipitate contrast when interacting with the neutrons. According to Eq. (19), this results in large precipitate volume fraction values. Since the concentration of iron in the precipitates is found to decrease with annealing time [14], the effective size of the iron shell decreases, giving rise to a continuous increase of  $\Delta\rho_{\text{NUC}}^2$  during annealing. This change in the contrast, however, would according to Eq. (19) lead to an unrealistic decrease of the precipitate volume fraction with time, even though in reality the vanadium-rich core is increasing in size. This evolution of the precipitate volume fraction is plotted in Fig. 12, curve I. The missing points in Fig. 12 are due to an interruption of the neutron beam. In this case, the precipitate profile can, for a certain moment of annealing, be mimicked as shown in Fig. 11 for the precipitate representation I.

For a quantitative analysis of the precipitate volume fraction evolution, one may consider an effective precipitate core with a homogenous composition that remains constant during annealing. The composition of the core can be for example, either the equilibrium composition as calculated by ThermoCalc, or the stoichiometric composition of the pure vanadium carbide (VC). The corresponding precipitate profiles in each case are depicted in Fig. 11, cases II and III, respectively. The effective precipitate size is described by the effective precipitate volume,  $V_{\text{eff}}$ , and in the case of ellipsoidal precipitates, by the two effective ellipsoidal radii,  $R_{\text{eq,eff}}$  and  $R_{\text{p,eff}}$ . In this way, when considering this effective precipitate size, i.e. the size of the precipitate core, an effective precipitate volume fraction,  $f_{\text{V,eff}}$ , can be obtained, which is related to  $f_{\text{V}}$  from Eq. (19):

$$f_{\text{V,eff}} = \frac{\Delta\rho_{\text{NUC}}^2}{\Delta\rho_{\text{NUC,eff}}^2} \cdot f_{\text{V}}. \quad (21)$$

In Eq. (21),  $\Delta\rho_{\text{NUC}}^2$  is the contrast of the  $(\text{Fe}_x\text{Mn}_z\text{V}_{1-x})\text{C}_y$  precipitates according to [14], and  $f_{\text{V}}$  is the corresponding volume fraction. The  $f_{\text{V,eff}}$  is the effective precipitate volume fraction corresponding to the  $\Delta\rho_{\text{NUC,eff}}^2$  used, for either the precipitates of representation II or III.

The fitting of Eq. (15) can be performed using either the nuclear contrast values,  $\Delta\rho_{\text{NUC,eff}}^2$ , for precipitates with the equilibrium composition that ThermoCalc predicts (representation II, Fig. 11) or the stoichiometric VC composition (representation III, Fig. 11). The values of  $\Delta\rho_{\text{NUC,eff}}^2$  used for all three steels are listed in Table 4.

The precipitate volume fraction resulting from the fit of the time evolution of the SANS intensity in the LCLV steel during annealing at 650 °C is shown as an example in Fig. 12 for the precip-

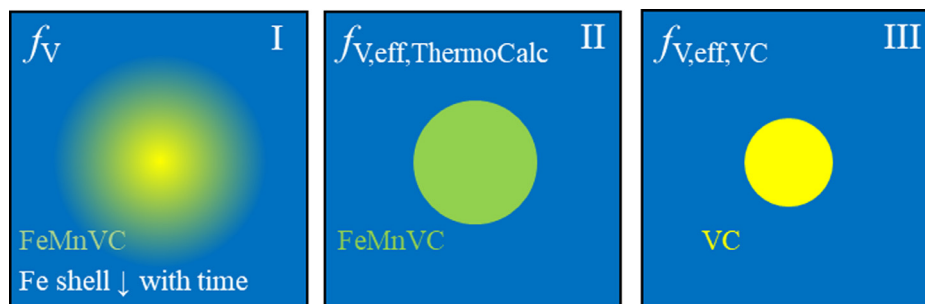


**Fig. 11.** Precipitate effective size and volume fraction at a certain moment of annealing. Precipitate representation I with volume fraction  $f_V$  and composition according to Ref. [14], precipitate representation II with effective volume fraction  $f_{V,eff,ThermoCalc}$  and equilibrium composition from ThermoCalc, and precipitate representation III with effective volume fraction  $f_{V,eff,VC}$  and composition of the stoichiometric vanadium carbide.

**Table 4**

The nuclear contrast values,  $\Delta\rho^2_{NUC,eff}$ , used to calculate the “effective” volume fraction of the precipitates with composition that ThermoCalc predicts (precipitate representation II, Fig. 11) and with the stoichiometric VC composition (precipitate representation III, Fig. 11) in all three steels.

| Steel | AnnealingT (°C) | $\Delta\rho^2_{NUC,eff}\times 10^{-7}$ nm <sup>-4</sup> case II | Precipitate composition by ThermoCalc  | $\Delta\rho^2_{NUC,eff}\times 10^{-7}$ nm <sup>-4</sup> case III | VC |
|-------|-----------------|---|--|--|----|
| LCLV  | 650             | 1.42  | (Fe <sub>0.156</sub> V <sub>0.84</sub> Mn <sub>0.006</sub> )C <sub>0.872</sub> | 1.88   | VC |
|       | 700             | 1.50  | (Fe <sub>0.133</sub> V <sub>0.86</sub> Mn <sub>0.004</sub> )C <sub>0.869</sub> | 1.85   | VC |
| LCHV  | 650             | 1.99  | (Fe <sub>0.049</sub> V <sub>0.95</sub> Mn <sub>0.001</sub> )C <sub>0.839</sub> | 1.88   | VC |
|       | 700             | 1.94  | (Fe <sub>0.050</sub> V <sub>0.95</sub> Mn <sub>0.001</sub> )C <sub>0.843</sub> | 1.85   | VC |
| HCHV  | 650             | 1.49  | (Fe <sub>0.140</sub> V <sub>0.86</sub> Mn <sub>0.005</sub> )C <sub>0.871</sub> | 1.88   | VC |
|       | 700             | 1.51  | (Fe <sub>0.130</sub> V <sub>0.87</sub> Mn <sub>0.004</sub> )C <sub>0.869</sub> | 1.85   | VC |

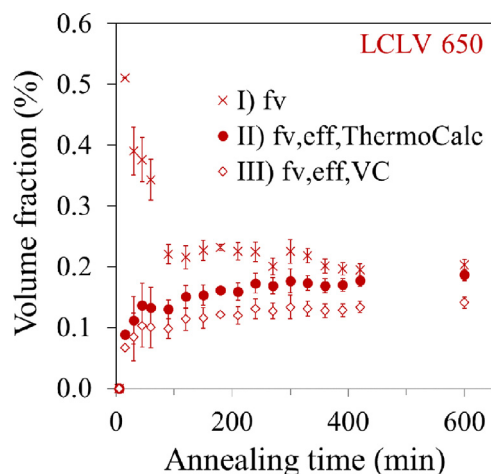


**Fig. 12.** Time evolution of the precipitate volume fraction in the LCLV alloy during annealing at 650 °C, calculated in different ways as described in the text. I, II and III sets correspond to the I, II and III precipitate representations of Fig. 11.

itate representations I, II and III. The precipitation kinetics of the precipitates of representations II and III show the same trend. The corresponding curves for the LCLV steel annealed at 700 °C and for the LCHV and HCHV steels annealed at both 650 and 700 °C are presented in the supplementary material of this article (Fig. S8).

In the following discussions, we refer to the precipitates of representation II, i.e. we present the precipitation kinetics of the effective volume fraction  $f_{V,eff,ThermoCalc}$ , and the corresponding radii and volume.

#### 4.b. SANS results and discussion

The precipitation kinetics in the LCLV, LCHV and HCHV steels during isothermal annealing at either 650 or 700 °C as obtained from the fitting of the  $(d\Sigma/d\Omega)_{NUC}(Q)$  is shown in Fig. 13a–i, where we depict the time evolution of the precipitate effective volume fraction (for precipitates with equilibrium composition from Ther-

moCalc), number density and size. The error bars in all plots originate from the fits of the SANS data and are thus related to the counting statistics. Therefore, the larger error bars at short annealing times, i.e. at the beginning of the isothermal holding, are due to the short time measuring times and the consequently lower counting statistics.

Precipitation takes place in all three steels at both annealing temperatures. The effective precipitate volume fraction increases during annealing in all cases, as shown in Fig. 13a–c, but the equilibrium volume fraction as calculated from ThermoCalc and presented in Table 5 is not reached in any of the steels. This means that after 10 h of annealing there is still supersaturation of vanadium in solid solution in the ferrite matrix. In the supplementary material of this article, we provide graphs (Fig. S9) showing the time evolution of the fraction of vanadium in solid solution and in the precipitates during annealing in all steels. At each annealing temperature, the final precipitate volume fraction after 10 h of annealing in the HCHV steel is approximately twice the corresponding volume fraction in the LCLV and LCHV alloys. The precipitate volume fraction in all steels is larger at 700 than at 650 °C during the entire annealing period of 10 h.

Comparable behavior is observed for the effective precipitate size. Fig. 13d–f and g–i show the increase in the precipitate size with annealing time and manifest the presence of larger precipitates at 700 °C in all steels. The precipitate shape is modeled as oblate ellipsoidal as explained above. The ratio  $R_{eq}/R_p$  is smaller at 650 °C than at 700 °C for all steels. The average  $R_{eq}/R_p$  ratio during annealing is 2.9, 3.0 and 2.9 for the LCLV, LCHV and HCHV steels at 650 °C, respectively, and 18.3, 12.3 and 5.4, for the LCLV, LCHV and HCHV steels at 700 °C, respectively.

According to the Zener model [49,50], the time evolution of the precipitate radius at the early stages of growth is given by:

$$R(t) \propto \sqrt{D_V(t - t_s)}, \quad (22)$$

where  $t$  is the time of annealing,  $t_s$  is the time when nucleation occurs and  $D_V$  is the diffusion coefficient of vanadium in the ferrite matrix. During this stage, the diffusion fields of the neighbor-

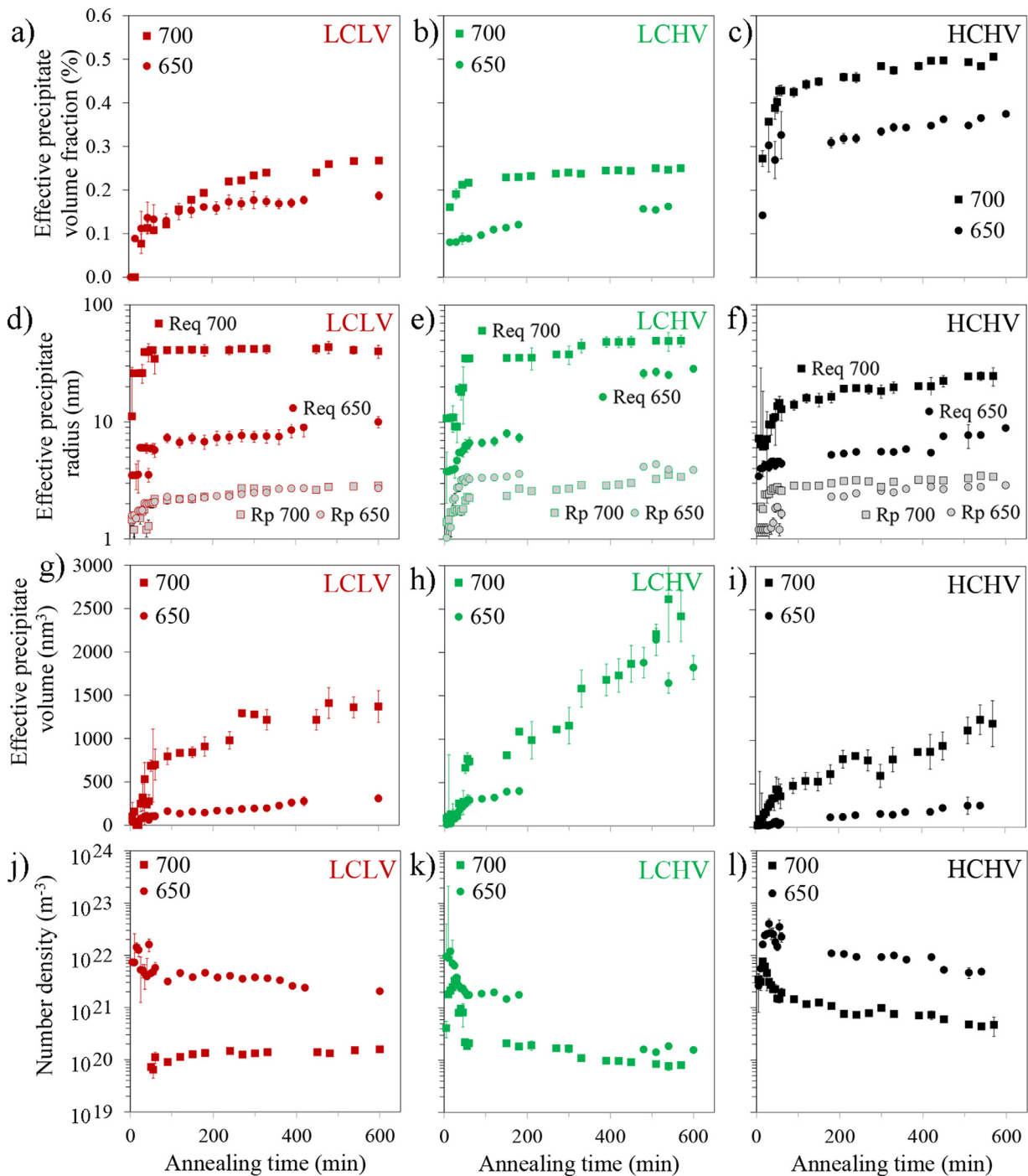


**Fig. 13.** Time evolution of the effective (a–c) volume fraction, (d–f) polar and equatorial mean radii, (g–i) volume and (j–l) number density of the precipitates in all steels during annealing at 650 and 700 °C.

ing precipitates do not overlap and coarsening does not take place. Since the diffusion coefficient of vanadium is larger at higher temperatures, for all steels the precipitates formed at 700 °C are larger than those formed at 650 °C.

The precipitate number density evolution in all alloys is shown in Fig. 13g–i. The number density is higher during the first minutes of annealing and gradually decreases after ~100 min. This implies that precipitate coarsening is taking place since the precipitate volume fraction is continuously rising during this period. The HCHV steel exhibits a larger volume fraction and number density of precipitates after 10 h of annealing compared to the LCLV and LCHV steels due to its higher vanadium and carbon concentrations.

In all steels, more precipitates are formed at 650 than at 700 °C. The driving force for nucleation of vanadium carbides in ferrite is calculated by ThermoCalc and is given for the three alloys and the two isothermal holding temperatures in Table 5. The nucleation rate of the precipitates,  $\dot{N}$ , depends on the driving force for precipitation [51]:

$$\dot{N} \propto \exp\left(-\frac{\Delta G^* + Q_D}{k_B T}\right). \quad (23)$$

In Eq. (23),  $T$  is the temperature,  $k_B$  the Boltzmann constant and  $Q_D$  the activation energy for the vanadium diffusion.  $\Delta G^*$  is the

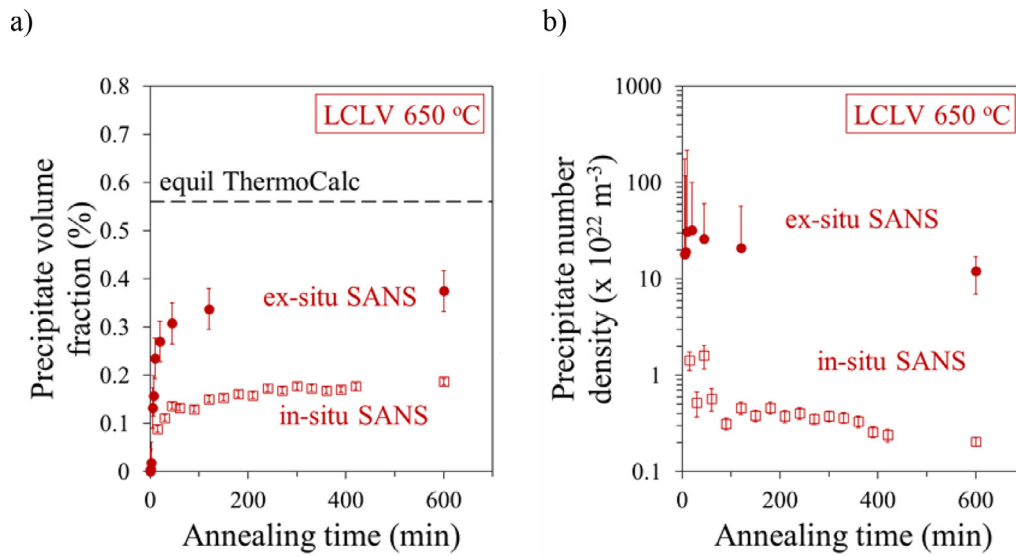


**Fig. 14.** Austenite to ferrite phase-transformation kinetics and precipitation kinetics during the 10 h isothermal annealing of the LCLV, LCHV and HCHV steels at 650 and 700 °C. The time evolution of the transformed austenite fraction, the precipitate volume fraction and number density are plotted.

activation energy for the nucleation of the precipitates described by [51]:

$$\Delta G^* = \frac{\Psi}{(\Delta G_V - g_s)^2}, \quad (24)$$

where  $\Delta G_V$  is the chemical driving force for the precipitate nucleation,  $g_s$  is the strain energy due to nucleation, and  $\Psi$  is a parameter containing details on the energies of the interfaces involved in nucleation and the shape of the nucleus [52].

Due to the larger driving force for precipitation when the isothermal annealing is performed at a lower temperature (Eq. (23)), a larger density of precipitates is observed at 650 °C. The presence of larger and fewer precipitates at 700 than at 650 °C in all steels is confirmed by TEM investigations (e.g. Fig. 10a and b referring to LCLV steel).

### 5. Interaction between the phase transformation and precipitation kinetics

*In-situ* simultaneous ND and SANS experiments have been performed in steels with different concentrations of vanadium and carbon. The coupling of the SANS to ND results allows studying the relation between the precipitation kinetics and phase-transformation kinetics during annealing at 650 or 700 °C. The time evolution of the size, number density and volume fraction of the precipitates in the LCLV, LCHV and HCHV steels is presented in Fig. 14, together with the evolution of the transformed austenite fraction in each steel at each annealing temperature.

As illustrated in Fig. 14, in all steels the precipitation takes place during and after the phase transformation and the precipitation kinetics follow the phase transformation kinetics. This indicates that the austenite to ferrite phase-transformation initiates the vanadium carbide precipitation. The precipitate number density at 650 °C is larger than at 700 °C, not only due to the larger driving force for precipitation at the lower temperature as explained above, but also due to faster phase-transformation kinetics at 650 °C. We also measure a higher precipitate growth rate and larger precipitates at 700 than at 650 °C (Fig. 13j–l) because of the faster diffusion of vanadium at the higher temperature. The slower phase-transformation kinetics at 700 °C may also lead to higher aspect ratios between the precipitate ellipsoidal radii,  $R_{eq}/R_p$ , because vanadium diffusion along the austenite/ferrite interface is

faster than perpendicular to the interface. This may lead to faster precipitate growth along the interface compared to growth perpendicular to the interface.

The promoted precipitation during the phase transformation is attributed to the solubility decrease of the vanadium and carbon when austenite transforms to ferrite, increasing the driving force for precipitation [5]. Since austenite to ferrite phase transformation takes place in all alloys at both temperatures, precipitates are detected in all cases.

The precipitate number density, size and volume fraction increase during austenite to ferrite phase transformation. This is an indication that the precipitation takes place at the migrating austenite/ferrite interface during the phase transformation, i.e. interphase precipitation. During phase transformation, the precipitate nucleation and growth are dominant over coarsening. When phase transformation is complete, the precipitate growth and coarsening are dominant since the precipitate number density does not increase while the precipitate size and volume fraction increase with time (Fig. 14). In all steels apart from the LCLV annealed at 700 °C, precipitate coarsening is observed since the number density decreases after having reached a maximum (Fig. 14a, c–f). The precipitation kinetics in the LCLV steel at 700 °C do not reach the coarsening stage (number density continuously increasing – Fig. 14b). This is attributed to the slow phase transformation kinetics in this steel at longer annealing times (Fig. 6d).

It is important to note that, even though the phase transformation is complete after 10 h of annealing of all three steels at both temperatures, the precipitation phenomenon is not complete.  $f_V$  has not reached a plateau but is continuously increasing (Fig. 13a–c). According to ThermoCalc calculations (Table 5, column 5), the precipitate volume fraction  $f_V$  has not reached the equilibrium value after 10 h of annealing.

In a previous study the precipitation kinetics in the LCLV and in the HCHV steels at 650 °C was measured by *ex-situ* SANS [16], in samples heat treated in a dilatometer before the SANS measurements. Differences are observed between the precipitation kinetics obtained by *in-situ* and *ex-situ* SANS in the same steels with the same heat-treatments. Since the applied magnetic field during the *in-situ* SANS measurements retards the austenite to ferrite phase transformation kinetics, and the phase transformation kinetics drive the precipitation kinetics, the different precipitation kinetics obtained by *in-situ* SANS are attributed to the effect of

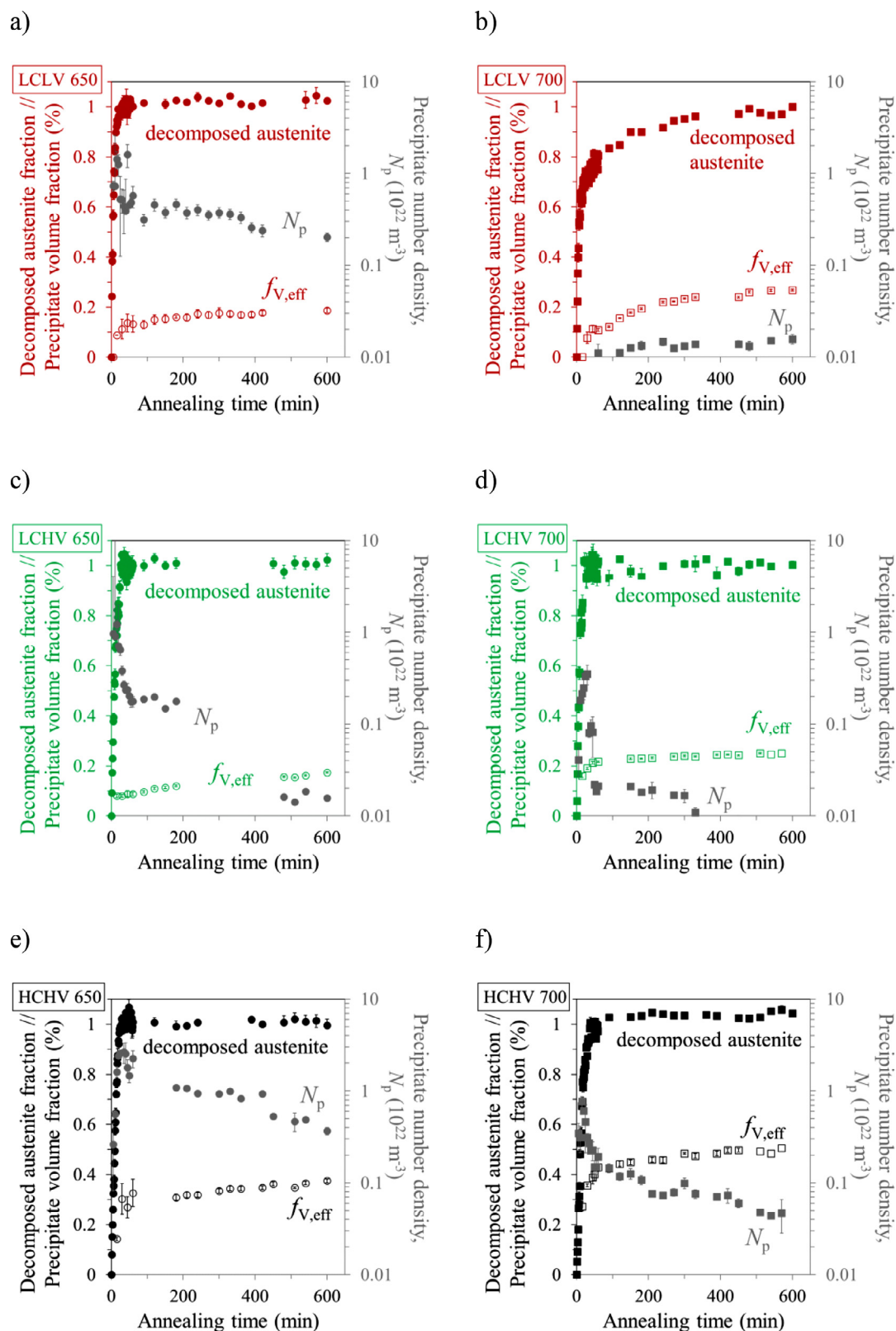


Fig. 15. Time evolution of the precipitate (a) volume fraction and (b) number density in the LCLV steel annealed at 650 °C, obtained by *ex-situ* SANS in dilatometry heat treated specimens and by *in-situ* SANS during the applied thermal cycle and under an external magnetic field of 1.5 T.

**Table 5**

Precipitate dissolution temperature,  $T_D$ , driving force for precipitation in ferrite,  $\Delta G_{V,p}$ , equilibrium precipitate volume fraction,  $f_{V,equl}$ , for the alloys of interest calculated by ThermoCalc, and measured volume fraction after 10 h of annealing,  $f_{V,eff - 10 h}$ .

| Steel | $T_D$ (°C) | AnnealingT (°C) | $\Delta G_{V,p}$ (kJ/mol) | $f_{V,equl}$ (%) | $f_{V,eff - 10 h}$ (%) |
|-------|------------|-----------------|---------------------------|------------------|------------------------|
| LCLV  | 990        | 650             | 24.3                      | 0.56             | 0.19                   |
|       | 990        | 700             | 21.0                      | 0.52             | 0.27                   |
| LCHV  | 1060       | 650             | 26.9                      | 0.64             | 0.16                   |
|       | 1060       | 700             | 23.7                      | 0.63             | 0.25                   |
| HCHV  | 1069       | 650             | 28.8                      | 1.08             | 0.37                   |
|       | 1069       | 700             | 25.8                      | 1.06             | 0.47                   |

the magnetic field. The retardation of phase transformation, i.e., the slower movement of the austenite/ferrite interface, results in a lower precipitate nucleation rate which leads to lower precipitate number densities and smaller precipitate volume fractions. These differences are presented in Fig. 15a and b for the LCLV alloy annealed at 650 °C as an example. Note here that the precipitation kinetics analysis for the *ex-situ* SANS measurements is performed considering VC carbide precipitates (representation III, Fig. 11).

Finally, regarding the precipitate size, larger precipitates are observed during the *in-situ* SANS measurements [16]. Slower phase-transformation kinetics leads to a higher accumulation of vanadium in the austenite/ferrite interface, thus, vanadium has time to diffuse into the precipitates and accelerate their growth. Since, as explained above, the accumulated vanadium atoms diffuse faster along the interface than perpendicular to it, higher aspect ratios between the precipitate ellipsoidal radii,  $R_{eq}/R_p$ , are promoted due to the slower phase-transformation kinetics when an external magnetic field is applied.

Since we observe that the precipitation kinetics are affected by an external magnetic field due to its effect on the phase transformation kinetics, the TEM analysis in the dilatometry heat-treated samples (without magnetic field) is used to obtain qualitative information on the precipitates shape, i.e. the precipitate shape can be modeled as ellipsoid. Quantitative information such as the aspect ratio between the precipitate ellipsoidal radii and the exact precipitate size are obtained from the fit of the SANS data.

Moreover, in a recent study [14], we measured the precipitates chemical composition evolution during annealing at 650 and 700 °C in the same LCLV, LCHV and HCHV alloys. We have observed faster increase in the vanadium metal fraction in the precipitates when increasing the alloying elements content, either the vanadium or the carbon concentration. Correlating this finding to the phase transformation and to the precipitation kinetics, the austenite to ferrite phase transformation is more sluggish when adding vanadium or carbon to the steel nominal composition, allowing more time for the vanadium to diffuse to the precipitates, increasing their vanadium concentration.

So far, the effect of the austenite to ferrite phase transformation kinetics on the precipitation kinetics is discussed. The effect of the precipitation on the phase transformation should also be addressed. The precipitation may affect the phase transformation in three ways [42]. The first is through the pinning force,  $P_z$ , that they induce which contributes to the reduction of the  $\alpha/\gamma$  interface velocity as described in Eqs. (6) and (7). The second effect originates from the fact that a fraction of vanadium is consumed in the precipitates, reducing the vanadium concentration in solid solution and weakening the solute drag effect due to vanadium, eventually promoting a higher phase transformation velocity. Adding vanadium to the steel nominal composition (comparison between LCLV and LCHV alloys), results in a higher vanadium concentration that is in solid solution (Fig. S9 in the supplementary material—see vanadium in solid solution the first minutes of annealing). Consequently, the energy dissipation due to the solute drag of vanadium is higher in the LCHV than in the LCLV steel

(Table 3), retarding the phase-transformation kinetics in the LCHV steel, compared to the LCLV steel. The third effect is related to the role of carbon. When interphase precipitation takes place, there is carbon consumption at the interphase boundary due to the precipitate formation. Therefore, there is no long-range diffusion of carbon, which otherwise would diffuse in the residual austenite, retarding the phase transformation kinetics.

## Conclusion

*In-situ* and simultaneous ND and SANS measurements in steels with different vanadium and carbon concentrations provide a unique insight into the interaction between the austenite to ferrite phase transformation and the precipitation kinetics during isothermal annealing at 650 and 700 °C. The conclusions of the *in-situ* studies are the following:

- Austenite to ferrite phase transformation is observed in all steels during annealing at 650 and 700 °C, and the transformation kinetics depends on the temperature and on the alloy composition. Faster kinetics at 650 than at 700 °C is measured in all alloys due to the larger driving force for phase transformation at lower temperatures.
- Additions of vanadium and carbon to the steel composition cause the retardation of the onset of phase transformation. At both temperatures, the net driving force for phase transformation is the largest for the low-carbon low-vanadium alloy, while adding vanadium or carbon to the steel causes a decrease in the net driving force, as a result of an increase in the energy dissipation due to vanadium solute drag.
- In all steels, the austenite-to-ferrite phase transformation initiates the vanadium carbide precipitation. This is attributed to the decrease of the solubility of vanadium and carbon when austenite transforms to ferrite, increasing the driving force for precipitation.
- The precipitate number density, size and volume fraction increase during the phase transformation in all steels, indicating that the precipitation takes place at the migrating austenite/ferrite interface during the phase transformation. After the completion of the phase transformation, the precipitates grow and coarsen. Larger and fewer ( $\sim 1-2$  orders of magnitude) precipitates are measured at 700 °C than at 650 °C in all steels, and a larger density of precipitates in the steel with the higher concentration of vanadium and carbon. The precipitate number density at 650 °C is higher than at 700 °C due to the larger driving force for precipitation and to the faster phase transformation kinetics at the lower temperature. The larger precipitate growth rate and the larger precipitate size is measured at 700 °C compared to 650 °C is attributed to the faster diffusion of vanadium at the higher temperature.
- Ellipsoidal precipitates are detected in all conditions, indicating faster precipitate growth along the austenite/ferrite interface than perpendicular to it because of the faster vanadium diffusion along the interface. The slower phase transformation



kinetics at 700 °C enable more time for the vanadium diffusion along the austenite/ferrite interface and lead to higher aspect ratios between the precipitate ellipsoidal radii. The polar radius  $R_p$  of the precipitates evolves in the range of 1–4 nm in all conditions, while the radius in the equatorial plane  $R_{eq}$  can reach maximum values from 10 to 50 nm, depending on the alloy and the annealing temperature.

- An interesting outcome is the delay in the onset and time evolution of the phase transformation due to the external magnetic field applied during the *in-situ* measurements, which consequently affects the precipitation kinetics, i.e. fewer and larger precipitates are formed. This once more confirms the coupling between the phase transformation and the precipitation kinetics.

Overall, our *in-situ* investigations provide quantitative information on the interaction of the austenite to ferrite phase-transformation kinetics with the vanadium-carbide precipitation kinetics. The outcome of this study can open new horizons in acquiring valuable quantitative data during the processing of steels with different compositions. The quantitative results can contribute to modeling and eventually predicting the precipitation and phase-transformation kinetics in steels which can lead to the optimization of steel design for automotive applications with reduced energy consumption.

### Declaration of Competing Interest

The authors declare that they have no known competing financial interests or personal relationships that could have appeared to influence the work reported in this paper.

### Acknowledgments

This work was financially supported by the Materials Innovation Institute M2i ([www.m2i.nl](http://www.m2i.nl)), Project S41.5.14548, in the framework of the M2i Partnership Program, and the Technology Foundation TTW ([www.stw.nl](http://www.stw.nl)), which is part of the Netherlands Organization for Scientific Research ([www.nwo.nl](http://www.nwo.nl)). The authors would like to acknowledge the use of the Larmor beamline at ISIS (Experiment No. RB1869024 [53]) and the Nederlandse Organisatie voor Wetenschappelijk Onderzoek Groot Grant No. LARMOR 721.012.102. The help of the support staff from ISIS during the neutron experiments is greatly acknowledged and very much appreciated. The authors are grateful to Tata Steel in Europe for providing the materials as hot-rolled plates. Finally, the authors thank Vitaliy Bliznuk for his assistance on TEM investigations in Ghent University.

### Supplementary materials

Supplementary material associated with this article can be found, in the online version, at doi:10.1016/j.actamat.2021.117317.

### References

- [1] K. Seto, Y. Funakawa, S. Kaneko, Hot rolled high strength steels for suspension and chassis parts "NANOHITEN and 'BHT® steel, *JFE Tech. Rep.* 10 (10) (2007) 19–25.
- [2] A. Rijkenberg, A. Blowey, P. Bellina, C. Wooffindin, Advanced high stretch-flange formability steels for chassis and suspension applications, in: *Proceeding of the Steels Cars Truck*, 2014, pp. 426–433. 2014.
- [3] Y. Funakawa, T. Shiozaki, K. Tomita, T. Yamamoto, E. Maeda, Development of high strength hot-rolled sheet steel consisting of ferrite and nanometer-sized carbides, *ISIJ Int.* 44 (11) (2004) 1945–1951, doi:10.2355/isijinternational.44.1945.
- [4] T.N. Baker, Microalloyed steels, *Ironmak. Steelmak.* 43 (4) (2016) 264–307, doi:10.1179/1743281215Y.0000000063.
- [5] T.N. Baker, Processes, microstructure and properties of vanadium microalloyed steels, *Mater. Sci. Technol.* 25 (9) (2009) 1083–1107, doi:10.1179/174328409X453253.

- [6] Z. S., B.H. Rune Lagneborg, Tadeusz Siwecki, Role of vanadium in microalloyed steels, *Stal* (12) (2001) 58–59.
- [7] P. Gong, X.G. Liu, A. Rijkenberg, W.M. Rainforth, The effect of molybdenum on interphase precipitation and microstructures in microalloyed steels containing titanium and vanadium, *Acta Mater.* 161 (2018) 374–387, doi:10.1016/j.actamat.2018.09.008.
- [8] G. Miyamoto, R. Hori, B. Poorganji, T. Furuahara, Interphase precipitation of VC and resultant hardening in V-added medium carbon steels, *ISIJ Int.* 51 (10) (2011) 1733–1739, doi:10.2355/isijinternational.51.1733.
- [9] Y.J. Zhang, et al., Effects of transformation temperature on VC interphase precipitation and resultant hardness in low-carbon steels, *Acta Mater.* 84 (2015) 375–384, doi:10.1016/j.actamat.2014.10.049.
- [10] Y.Q. Wang, et al., Investigating nano-precipitation in a V-containing HSLA steel using small angle neutron scattering, *Acta Mater.* 145 (2018) 84–96, doi:10.1016/j.actamat.2017.11.032.
- [11] Y. Oba, et al., Quantitative analysis of precipitate in vanadium-microalloyed medium carbon steels using small-angle X-ray and neutron scattering methods, *ISIJ Int.* 51 (11) (2011) 1852–1858, doi:10.2355/isijinternational.51.1852.
- [12] S. Shanmugam, M. Tanniru, R.D.K. Misra, D. Panda, S. Jansto, Microalloyed V-Nb-Ti and V steels part 2-precipitation behavior during processing of structural beams, *Mater. Sci. Technol.* 21 (2) (2005) 165–177, doi:10.1179/174328405X18656.
- [13] Thierry Epicier, Daniel Acevedo-Reyes, M. Perez, Crystallographic structure of vanadium carbide precipitates in a model Fe-C-V steel, *Int. J. Prod. Res.* 23 (2010) 1–36 september.
- [14] C. Ioannidou, et al., Evolution of the precipitate composition during annealing of vanadium micro-alloyed steels by *in-situ* SANS, *Acta Mater.* 201 (2020) 217–230, doi:10.1016/j.actamat.2020.09.083.
- [15] M. Nöhrer, S. Zamberger, S. Primig, H. Leitner, Atom probe study of vanadium interphase precipitates and randomly distributed vanadium precipitates in ferrite, *Micron* 54–55 (2013) 57–64, doi:10.1016/j.micron.2013.08.008.
- [16] C. Ioannidou, et al., Interaction of precipitation with austenite-to-ferrite phase transformation in vanadium micro-alloyed steels, *Acta Mater.* 181 (2019) 10–24, doi:10.1016/j.actamat.2019.09.046.
- [17] C. Ioannidou, Z. Arechabaleta, A. Rijkenberg, R.M. Dalgliesh, A.A. van Well, S.E. Offerman, VC-precipitation kinetics studied by small-angle neutron scattering in nano-steels, *Mater. Sci. Forum* 941 (2018) 236–244 MSF, doi:10.4028/www.scientific.net/MSF.941.236.
- [18] M.Y. Chen, M. Gouné, M. Verdier, Y. Bréchet, J.R. Yang, Interphase precipitation in vanadium-alloyed steels: strengthening contribution and morphological variability with austenite to ferrite transformation, *Acta Mater.* 64 (2014) 78–92, doi:10.1016/j.actamat.2013.11.025.
- [19] Y.J. Zhang, G. Miyamoto, K. Shinbo, T. Furuahara, Effects of  $\alpha/\gamma$  orientation relationship on VC interphase precipitation in low-carbon steels, *Scr. Mater.* 69 (1) (2013) 17–20, doi:10.1016/j.scriptamat.2013.03.020.
- [20] G. Miyamoto, R. Hori, B. Poorganji, T. Furuahara, Crystallographic analysis of proeutectoid ferrite/austenite interface and interphase precipitation of vanadium carbide in medium-carbon steel, *Metall. Mater. Trans. A* 44 (8) (2013) 3436–3443 Phys. Metall. Mater. Sci., doi:10.1007/s11661-013-1702-2.
- [21] Y.J. Zhang, G. Miyamoto, K. Shinbo, T. Furuahara, Quantitative measurements of phase equilibria at migrating  $\alpha/\gamma$  interface and dispersion of VC interphase precipitates: evaluation of driving force for interphase precipitation, *Acta Mater.* 128 (2017) 166–175, doi:10.1016/j.actamat.2017.02.020.
- [22] X. Zhang, et al., Microstructure, precipitate and property evolution in cold-rolled Ti-V high strength low alloy steel, *Mater. Des.* 192 (2020), doi:10.1016/j.matdes.2020.108720.
- [23] S. Dhara, R.K.W. Marceau, K. Wood, T. Dorin, I.B. Timokhina, P.D. Hodgson, Precipitation and clustering in a Ti-Mo steel investigated using atom probe tomography and small-angle neutron scattering, *Mater. Sci. Eng. A* 718 (2018) 74–86 November 2017, doi:10.1016/j.msea.2018.01.070.
- [24] A. Navarro-López, et al., Furnace for in situ and simultaneous studies of nano-precipitates and phase transformations in steels by SANS and neutron diffraction, *Rev. Sci. Instrum.* 91 (12) (2020), doi:10.1063/1.50022507.
- [25] J.O. Andersson, T. Helander, L. Höglund, P.F. Shi, B. Sundman, Thermo-calc and DICTRA, computational tools for materials science, *Calphad* 26 (2002) 273–312 [Online]. Available: Andersson J.O., Helander T., Höglund L., Shi P.F., and Sundman B., (2002), Thermo-Calc and DICTRA, Computational tools for materials science. *Calphad*, 26, 273–312.
- [26] . <https://www.isis.stfc.ac.uk/Pages/Larmor.aspx>.
- [27] . <https://www.isis.stfc.ac.uk/Pages/home.aspx>.
- [28] O. Arnold, et al., Mantid-data analysis and visualization package for neutron scattering and  $\mu$  SR experiments, *Nucl. Instrum. Methods Phys. Res. Sect. A Accel. Spectrom. Detect. Assoc. Equip.* 764 (2014) 156–166, doi:10.1016/j.nima.2014.07.029.
- [29] L. Van Eijck, et al., Design and performance of a novel neutron powder diffractometer: PEARL at TU Delft, *J. Appl. Crystallogr.* 49 (5) (2016) 1398–1401, doi:10.1107/S160057671601089X.
- [30] N. Yano, T. Yamada, T. Hosoya, T. Ohhara, I. Tanaka, K. Kusaka, Application of profile fitting method to neutron time-of-flight protein single crystal diffraction data collected at the iBIX, *Sci. Rep.* 6 (2016) 4–12 August, doi:10.1038/srep36628.
- [31] M. Avrami, Kinetics of phase change. I: general theory, *J. Chem. Phys.* 7 (12) (1939) 1103–1112, doi:10.1063/1.1750380.
- [32] J.W. Cahn, The kinetics of grain boundary nucleated reactions, *Acta Metall.* 4 (5) (1956) 449–459, doi:10.1016/0001-6160(56)90041-4.

- [33] E.G. Dere, Microstructure Control of fire-resistant, low-alloy steel, an *in-situ* 3D X-ray diffraction and small-angle X-ray scattering study, Phd Thesis TUDelft (2013).
- [34] G.P. Krielaart, S. Van Der Zwaag, Kinetics of  $\gamma \rightarrow \gamma'$  phase transformation in Fe-Mn alloys containing low manganese, *Mater. Sci. Technol.* 14 (1) (1998) 10–18, doi:10.1179/mst.1998.14.1.10.
- [35] V. SHAH, M. KRUGLA, S.E. OFFERMAN, J. SIETSMAN, D.N. HANLON, Effect of silicon, manganese and heating rate on the ferrite recrystallization kinetics, *ISIJ Int.* 60 (6) (2020) 1312–1323, doi:10.2355/isijinternational.ISIJINT-2019-475.
- [36] Q. Yong, X. Sun, Z. Li, Z. Wang, K. Zhang, Physical metallurgical principles of titanium microalloyed steel—dissolution and precipitation of titanium-bearing secondary phases, in: X. Mao (Ed.), *Titanium Microalloyed Steel: Fundamentals, Technology, and Products*, Ed, Springer, Singapore, 2019, pp. 71–139.
- [37] M. Hillert, Diffusion and interface control of reactions in alloys, *Metall. Trans. A* 6 (1) (1975) 5–19, doi:10.1007/BF02673664.
- [38] H. Guo, M. Enomoto, Effects of substitutional solute accumulation at  $\alpha/\gamma$  boundaries on the growth of ferrite in low carbon steels, *Metall. Mater. Trans. A* 38 (6) (2007) 1152–1161 *Phys. Metall. Mater. Sci.*, doi:10.1007/s11661-007-9139-0.
- [39] H. Chen, K. Zhu, L. Zhao, S. Van Der Zwaag, Analysis of transformation stasis during the isothermal bainitic ferrite formation in Fe-C-Mn and Fe-C-Mn-Si alloys, *Acta Mater.* 61 (14) (2013) 5458–5468, doi:10.1016/j.actamat.2013.05.034.
- [40] S. Clark, V. Janik, Y. Lan, S. Sridhar, Interphase precipitation - an interfacial segregation model, *ISIJ Int.* 57 (3) (2017) 524–532, doi:10.2355/isijinternational.ISIJINT-2016-544.
- [41] R. Okamoto, J. Agren, A model for interphase precipitation based on finite interface solute drag theory, *Acta Mater.* 58 (2010) 4791–4803, doi:10.1016/j.actamat.2010.05.016.
- [42] H. Dong, et al., Unraveling the effects of Nb interface segregation on ferrite transformation kinetics in low carbon steels, *Acta Mater.* (2021) 117081, doi:10.1016/j.actamat.2021.117081.
- [43] M. Enomoto, H. Guo, Y. Tazuke, Y.R. Abe, M. Shimotomai, Influence of magnetic field on the kinetics of proeutectoid ferrite transformation in iron alloys, *Metall. Mater. Trans. A* 32 (3) (2001) 445–453 *Phys. Metall. Mater. Sci.*, doi:10.1007/s11661-001-0061-6.
- [44] H. Fujii, Effects of magnetic-field on elemental process for microstructural development of iron-based polycrystalline materials, Ph.D thesis, Tohoku University, 2009.
- [45] T. Narayanan, Synchrotron small-angle X-ray scattering studies of colloidal suspensions, in: M. Gomez, A. Nogales, M.C. Garcia-Gutierrez, T.A. Ezquerro (Eds.), *Applications of Synchrotron Light to Scattering and Diffraction in Materials and Life Sciences*, Eds, Springer, Berlin Heidelberg, 2009, pp. 133–156.
- [46] A. Wiedenmann, T. Chatterji, CHAPTER 10 - small angle neutron scattering investigations of magnetic nanostructures, in: *Neutron Scattering from Magnetic Materials*, Ed, Elsevier Science, Amsterdam, 2006, pp. 473–520.
- [47] L.A. Feigin, D.I. Svergun, G.W. Taylor, Determination of the integral parameters of particles, in: G.W. Taylor (Ed.), *Structure Analysis by Small-Angle X-Ray and Neutron Scattering*, Ed, Springer US, Boston, MA, 1987, pp. 59–105.
- [48] SasView, SasView for small angle scattering analysis. <http://www.sasview.org/index.html>, 2017. Accessed 4th January 2017.
- [49] S.G.E. Te Velthuis, N.H. Van Dijk, M.T. Rekveldt, J. Sietsma, S. Van Der Zwaag, A three-dimensional model for the development of the microstructure in steel during slow cooling, *Mater. Sci. Eng. A* 277 (1–2) (2000) 218–228, doi:10.1016/S0921-5093(99)00531-6.
- [50] C.E.I.C. Ohlund, J. Weidow, M. Thuvander, S.E. Offerman, Effect of Ti on evolution of microstructure and hardness of martensitic Fe-C-mn steel during tempering, *ISIJ Int.* 54 (12) (2014) 2890–2899, doi:10.2355/isijinternational.54.2890.
- [51] H. Sharma, J. Sietsma, S.E. Offerman, Preferential nucleation during polymorphic transformations, *Sci. Rep.* 6 (August) (2016) 1–7, doi:10.1038/srep30860.
- [52] by S.E. Offerman, et al.S.E. Offerman, et al. (Eds.), Reply to the discussion by Aaronson et al. to 'grain nucleation and growth during phase transformations', *Scr. Mater.* 51 (9) (2004) 937–941, doi:10.1016/j.scriptamat.2004.06.031.
- [53] S.E. Offerman, E. van der Wal, A.A. van Well, C. Ioannidou, A. Navarro-López, R.M. Dalglish, *In-situ* and simultaneous SANS and ND to study the precipitation and phase transformation kinetics in V-containing nano-steels, STFC ISIS Neutron Muon Source (2019), doi:10.5286/ISIS.E.100757775.